Molecular Dynamics-based Approaches for Mesoscale Lubrication

by

Nisha Chandramoorthy

B.Tech., Indian Institute of Technology Roorkee (2014)

Submitted to the School of Engineering
in partial fulfillment of the requirements for the degree of

Master of Science in Computation for Design and Optimization

at the

MASSACHUSETTS INSTITUTE OF TECHNOLOGY

September 2016

Signature redacted

Author .....
School of Engineering
August 5th, 2016

Signature redacted

Certified by .....
Nicolas G. Hadjiconstantinou
Professor, Department of Mechanical Engineering
Thesis Supervisor

Signature redacted

Accepted by .....
Youssef Marzouk
Associate Professor, Department of Aeronautics and Astronautics and
Co-director, Computation for Design and Optimization

Molecular Dynamics-based Approaches for Mesoscale Lubrication

by

Nisha Chandramoorthy

Submitted to the School of Engineering
on August 5th, 2016, in partial fulfillment of the
requirements for the degree of
Master of Science in Computation for Design and Optimization

Abstract

Classical lubrication theory is unable to describe nanoscale flows due to the failure of two of its constitutive components: a) the Newtonian stress-strain rate relationship and b) the no-slip boundary condition. In this thesis, we present a methodology for deriving a modified Reynolds equation (referred to as the Molecular Dynamics-based Equation for Lubrication, or the MODEL) which overcomes these limitations by introducing a Molecular Dynamics-based constitutive relationship for the flow rate through the lubrication gap, that is valid beyond the range of validity of the Navier-Stokes constitutive models. We demonstrate the proposed methodology for the flow of a simple lubricant, n-hexadecane, between smooth Iron walls and show that the MODEL is able to predict flow rates with good accuracy even in nanochannels that are only a few atomic layers wide. The MODEL constitutive relationship for the flow rate used in this work is a slip-corrected Poiseuille model with the slip length and viscosity derived from Molecular Dynamics (MD) simulations of pressure-driven flow in nanochannels sufficiently large that the Navier-Stokes description is valid. Although more general expressions for the flow rate can certainly be used, for the lubricant-solid system modeled here, the slip-corrected Poiseuille flow was surprisingly found to be sufficient.

We validate the MODEL by comparing MD results for the pressure distribution in a barrel-drop lubrication configuration with the analytical solution for the pressure obtained by solving the MODEL. The excellent agreement obtained between the dynamic pressure in the fluid measured from these MD simulations and the MODEL results suggests that it is possible to extend pde-based hydrodynamic modelling of lubrication problems even to nanoscale films beyond the validity of the Navier-Stokes description. In other words, once the flow rate constitutive relation is obtained, lubrication problems in nanoscale films can be solved without resorting to expensive particle methods like MD.

We demonstrate that slip cannot be neglected in the boundary lubrication regime by considering various lubrication problems of practical interest. Using a simple barrel-drop lubrication model for the top two rings in an internal combustion engine,

we show that for lubrication gaps with a minimum thickness that is ten times the size of the slip length, the normal force and the frictional force are overestimated by a factor of 1.5 when assuming no-slip.

By modifying the Twin Land Oil Control Ring (TLOCR)-liner interface model to include slip, we find significant reduction in the hydrodynamic pressure and the friction when compared to the original model; the oil flow rate does not change appreciably. Finally, we chalk out a procedure for the inclusion of slip in the methodology for developing correlations for the pressure, friction and the flow rate in the TLOCR-liner system.

Thesis Supervisor: Nicolas G. Hadjiconstantinou
Title: Professor, Department of Mechanical Engineering

Acknowledgments

I consider myself extremely lucky to have been advised by Professor Nicolas Hadjiconstantinou and think it is difficult to write a short thank you note befitting the extraordinarily generous amount of time and effort he invested into helping me. I am really grateful to him for having given me the idea of leveraging Molecular Dynamics (MD) flow rates to derive a mesoscale Reynolds-type equation, at a time when my ideas for a coarse-grained particle-based method for interfacial flows were only slightly better than daydreams. I greatly admire his physical intuition and insight and I am more than thankful for all his patient explanations which served as the largest reference while writing this thesis. His emphasis on looking for the simplest solutions first and on correctly interpreting numerical results, have taught me valuable lessons. What I am most grateful to him for is inspiring me by being meticulous, right from carefully analyzing MD results with me, to helping me edit every piece of writing for clarity and precision. I have to admit that on several occasions in the last two years, I have been astounded by Professor Hadjiconstantinou's patience, willingness to help and his perennial stash of humorous quips. My sincerest thanks to him!

I would like to thank Dr. Tian Tian for making the inclusion of slip effects in the piston ring-liner models (chapter 5 and parts of chapter 4) possible. He has been extremely kind in clarifying my doubts and providing me with the TLOCR program developed in his group, which I have used in this thesis. I would like to thank Yang Liu for helping me understand the correlation method and answering my questions patiently. I would also like to thank Haijie Chen and Yong Li, past members of the Sloan Automotive Lab, whose well-written code and theses simplified the process of extending their work and Yuwei Li, for introducing me to the barrel-drop lubrication problem.

This work was sponsored by the Consortium on Lubrication in Internal Combustion Engines with additional support from Argonne National Laboratory and the US Department of Energy. The current consortium members are Daimler, Mahle, MTU Friedrichshafen, PSA Peugeot Citroën, Renault, Shell, Toyota, Volkswagen, Volvo

Cars, Volvo Trucks, and Weichai Power. I am very grateful to the Consortium for motivating new directions for further work, at the periodic meetings. I would also like to thank the Center for Nanoscale Materials, Argonne National Laboratory, for giving me access to their computing facilities, without which this thesis could not have been completed. The use of the Center for Nanoscale Materials, an Office of Science user facility, was supported by the U. S. Department of Energy, Office of Science, Office of Basic Energy Sciences, under Contract No. DE-AC02-06CH11357.

I am eternally grateful to Dr. Mary-Catherine Kropinski, Dr. Praveen Chandrashekar and Dr. Karthik Duraisamy for initiating my education in computational methods for fluid dynamics. Little did I know that my innocent email to Dr. Kropinski seeking an internship would be life-changing in many ways; She has been the best mentor I could have hoped for and is one of the most amazing people I am lucky to know. I would like to thank my friends Gerald Wang and Mathew Swisher, for numerous insightful discussions and always being ready with ideas to fix simulation errors. Our constant prattle, mediated by noises from computers at various stages of assembly/evolution, not only helped me learn a little statistical physics, but also kept my spirits up. Many thanks to my best friend Nandhini Chandramoorthy for relentlessly knocking down my existential crises and also for coming up with the acronym MODEL, Tuhin Sarkar for helping me get through some difficult times, and Ali Yawar, Akshay Agarwal, Karthik Swaminathan and Mojtaba Forghani Oozroody for many a timely motivational speech. Finally, I would like to thank my parents, Hema Sundaresan and V. S. Chandramoorthy, for their support and faith.

Contents

List of Figures

List of Tables

Chapter 1

Introduction

This thesis is concerned with the application of molecular/atomistic modelling techniques to the field of lubrication in internal combustion (IC) engines. The field of IC engines is quite mature and many expository studies have been performed on all aspects of lubrication encountered in this application. See for example, [4, 17] for latest work on lubricant composition, Müser's works for recent theoretical models for friction [80], [66, 22] for state-of-the-art modelling of piston-ring dynamics, [59, 58] for current progress in understanding tribological mechanisms under different wear conditions and [70] for multi-scale modelling in lubrication. However, the ever increasing drive for developing more efficient engines with reduced emissions [55, 95, 34, 78] as well as understanding the physics behind such performance, continually challenges the limits of applicability of these models.

One manifestation of this interplay that is of particular scientific interest is the breakdown of the traditional continuum modelling tools as lubrication gaps become very small. This is a subject that has attracted considerable attention in the scientific literature. See [91] for a review up to the last decade and [82, 115, 116, 69, 112] for recent thin-film friction and lubrication studies. Although some progress has been made, a considerable number of questions remain open. Additionally, the majority of this research has been performed in abstract settings with little connection, if any, to practical applications, such as lubrication in IC engines.

In this thesis, we attempt to provide answers to some of these questions in the

context of lubrication in IC engines. Specifically, we limit ourselves to the case of small lubrication gaps with no contact and examine whether continuum descriptions that extend traditional lubrication theory beyond its nominal validity limits are possible. The answer to that question can be found in this thesis.

1.1 Background

1.1.1 Boundary lubrication

Starting with the works of Dowson [26], fluid film lubrication in the hydrodynamic regime (where film thicknesses are on the order of microns or larger) is now thoroughly understood. Following the pioneering work of Dowson and Higginson on Elasto-Hydrodynamic Lubrication (EHL) theory, the coupling between hydrodynamic pressures and elastic deformations of the bounding surfaces is also well understood now [27, 44, 43, 42].

One of the regimes currently receiving considerable scientific interest is *boundary lubrication* [91, 8], in which the lubricant film thickness is comparable to the length scale of the surface roughness of the confining solids. Due to the development of extremely high pressures [94], in boundary lubrication, films that are a few atomic layers thick can, in some cases, be displaced, resulting in contact between solid surfaces. At the same time, continuum models which form the basis for hydrodynamic and EHL theory, begin to fail at small scales (e.g. gap heights $\lesssim 0.1\mu m$) [91, 69] typical of boundary lubrication. In other words, boundary lubrication is a multiscale fluid-structure interaction problem, combining hydrodynamics with elasticity, contact and wear (material transfer), all at scales sufficiently small that the traditional continuum treatments and models do not hold.

Fortunately, advances in computing capabilities and the availability of particle simulation techniques like Molecular Dynamics (MD), have recently enabled studies [104, 103, 102, 7, 94, 50, 9] of boundary lubrication. In this thesis we take advantage of these capabilities to study one aspect of this multifaceted problem, namely the

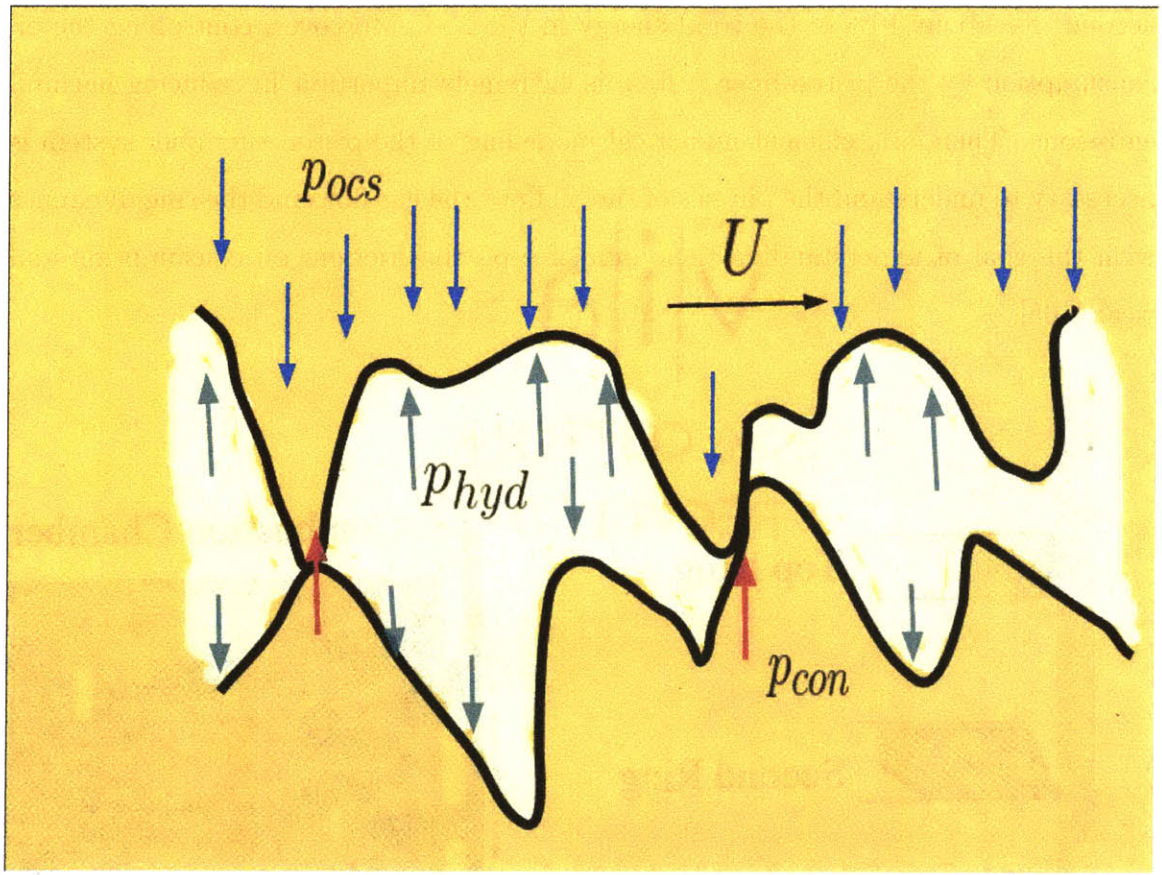

Figure 1-1: A schematic of a boundary lubricated contact. The thickness of the lubricant film (shown in white), is comparable to the asperity heights in the solid surfaces. In a typical lubricated contact, an external load exerts a pressure p_{ocs} (which represents the pressure supplied by the oil control spring, in case of the Twin Land Oil Control Ring-liner system) on the solid that is counteracted by the force due to the hydrodynamic pressure in the film, p_{hyd} and the contact pressure p_{con}.

breakdown of the Navier-Stokes description for small (lubrication) gap heights.

1.1.2 IC engines and the scope of the present work

In this section we briefly introduce the specific context and geometry of the piston ring pack-liner system in IC engines that we will concern ourselves with. More thorough discussions of lubrication in IC engines, with particular emphasis on the piston ring pack-liner system can be found in [105, 106, 96, 20, 67].

Frictional losses at the piston ring-liner interface constitute a significant portion, $20 - 50\%$, of the total friction loss in IC engines [105, 20]. The total friction losses

account for about 10% of the total energy in the fuel. Moreover, controlling the oil consumption by the piston-liner system is extremely important in reducing harmful emissions. Therefore, efficient numerical modelling of the piston ring-liner system is necessary to understand the physics of the oil flow, the gas flow and the ring dynamics with the goal of understanding their influence on the friction, oil consumption and wear [105].

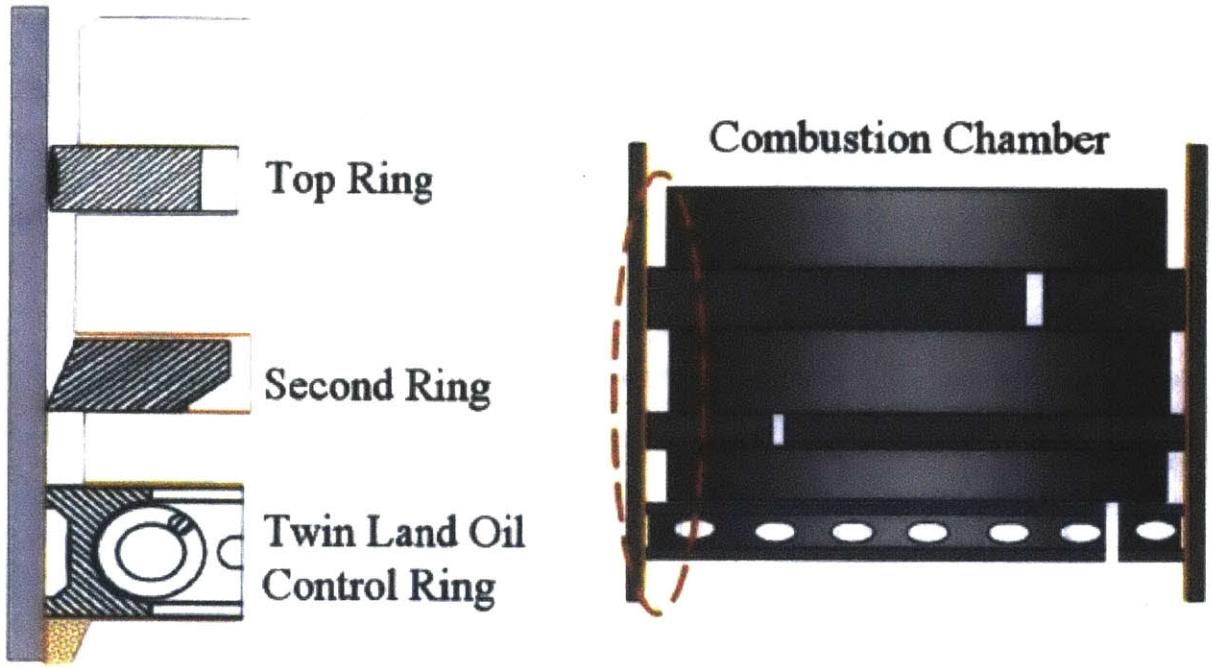

Figure 1-2: Schematic of the Piston Ring Pack. Courtesy of Liu [67]. The left hand side figure shows the vertical cross-sectional view of the contact plane.

The schematic in Figure 1-2 shows the most common configuration of a piston with 3 rings, and the cylinder liner. Figure 1-2 shows the Twin Land Oil Control Ring (TLOCR) which controls the oil available to the top two rings, called the compression and groove rings. The top two rings are responsible for sealing off combustion gases in the combustion chamber, improving the heat transfer from the piston to the cylinder wall and to both lubricate and scrape down oil from the cylinder wall [75].

The piston ring pack system has been the subject of some sophisticated theoretical analyses that have also been immensely useful in practical design improvements [105, 20, 76, 88]. The phenomenon of cavitation at pockets of low fluid pressure,

which presented great modelling challenges over the last few decades, has been rigorously incorporated into these analyses. Equally meticulous is the consideration of the composite micro-roughness of the liner surface in the numerical methods for the solution presented in these works. In this thesis, we are concerned with including interfacial slip effects that had been neglected so far in these piston ring pack studies.

Due to a 3-stage honing process, some portions of the liner surface consist of valleys that are several microns deep while some other portions, that undergo a finer honing stage, have an RMS roughness in the nanometer range [20, 67]. This portion of the liner surface with its fine roughness in the nanometer range is called the *plateau* region. Conditions of boundary lubrication are most likely to be observed in the gap between the plateau regions of the liner and the ring surface. The properties of the plateau roughness are characterized by Ra and σ_p, which are the mean and standard deviations of the absolute values of the statistical deviations from the mean liner surface level.

Since experimental measurements of the surface roughness are difficult to obtain, we model patches of the liner plateau region, where surface measurements are available. These representative patches are referred to as *phases* [67, 20]. The top two rings considered in chapter 4 are approximated to have a parabolic profile in the contact plane, while the TLOCR, considered in chapter 5, has a nominally flat surface. All three rings have a surface roughness that is an order of magnitude smaller than the liner roughness. Hence, they are considered smooth in comparison.

1.2 Thesis overview

In the next chapter we introduce Molecular Dynamics (MD) as the tool of choice for obtaining insight into boundary lubrication and in particular the hydrodynamics of lubrication at small scales. We also discuss simulation set up and methodology for the Non-Equilibrium Molecular Dynamics (NEMD) simulations discussed in the subsequent chapters of this thesis.

In chapter 3 we introduce a method for leveraging flow rate information from MD

simulations of nanochannel flows to obtain a continuum hydrodynamic model for describing lubrication problems at lengthscales at which the traditional Navier-Stokes descrption is not valid. The resulting method is referred to as MODEL (Molecular Dynamics-based Equation for Lubrication) and serves as a replacement to the classical Reynolds equation for boundary lubrication problems at nanoscale gap heights (excluding contact).

In chapter 4 we discuss the effect of slip in the context of piston ring-liner lubrication, using a simplified *barrel-drop* model. We also validate the MODEL derived in chapter 3 by comparing the analytical solutions of the barrel-drop model with MD simulations.

In chapter 5 we modify Chen's [20] Twin-Land Oil Control Ring (TLOCR) model to include slip. We propose that the solutions of the modified deterministic solver be parametrized by the slip length (in addition to the parameters in the existing models) and used to augment Chen's correlation method.

In the final chapter we summarize our results and provide direction for future work.

Chapter 2

Molecular Dynamics for Nanohydrodynamic Lubrication Simulations

In this thesis we make extensive use of MD simulations to obtain molecular insight into the behavior of nanoconfined fluids and the resulting failure of the Navier-Stokes description. MD is the most suited among *dense-fluid* simulation methods to the task at hand. Coarse-grained methods, such as Lattice Boltzmann [23] and Dissipative Particle Dynamics [46], are more efficient, but make crucial approximations of local Navier-Stokes behavior, which disqualify them from consideration. Quantum-based ab-initio molecular simulation methods [93] can be expected to provide more realistic modelling of material constitutive behavior at the expense of severe computational cost; in other words, such methods are simply too expensive to simulate systems sufficiently large to observe collective hydrodynamic behavior, which is our interest here.

Due to the enormous number of molecules present, even in small systems, only nanoscale systems can be simulated with MD using conventional computational resources. Fortunately, our interest lies precisely in these small systems. Moreover, the "art" of molecular simulation, developed over the last few decades, teaches us how to judiciously use periodic boundary conditions and/or other system termination meth-

ods, as well as exploit the fact that such small systems have short characteristic evolution times to simulate systems that would normally be considered beyond the reach of our computational resources.

Below, we proceed with an introduction to MD simulation, followed by a more detailed exposition of the methodology used to simulate the systems of interest to the present thesis work.

2.1 Introduction

In Molecular Dynamics, the dynamics of a system consisting of an ensemble of atomic particles is studied by numerically integrating Newton's laws of motion for each particle, using prescribed interatomic potentials [3]. The method used here is the standard Velocity Verlet time integration scheme [108, 109, 64]. In this scheme, the position $\mathbf{r}_i$ and velocity, $\mathbf{v}_i$, of the ith particle, $i \in \{1, 2, \cdots N\}$ is updated every timestep as follows:

$$\mathbf{r}_i(t+\delta t) = \mathbf{r}_i(t) + \mathbf{v}_i(t)\delta t + \frac{1}{2}\delta t^2 \mathbf{a}_i(t)$$
$$\mathbf{v}_i(t+\delta t) = \mathbf{v}_i(t) + \frac{\delta t}{2}\Big(\mathbf{a}_i(t) + \mathbf{a}_i(t+\delta t)\Big)$$

where, $\mathbf{a}_i(t)$ is the acceleration of a particle, determined from

$$\begin{aligned} m_i \mathbf{a}_i(t) = &- \sum_{i_1 \neq i} \nabla_i \phi_1(r_{ii_1}) - \sum_{i_1 \neq i} \sum_{i_2 \neq i, i_1} \nabla_i \phi_2(r_{ii_1}, r_{ii_2}, \theta_{ii_1 i_2}) \\ &- \cdots - \sum_{i_1 \neq i} \sum_{i_2 \neq i, i_1} \cdots \sum_{i_{k-1} \neq \{i, i_1 \ldots i_{k-2}\}} \nabla_i \phi_{k-1}(r_{ii_1}, \cdots, r_{i(k-1)}, \theta_{ii_1 i_2}, \cdots, \theta_{ii_{k-2} i_{k-1}}) \\ &+ F_i^{ext}(\mathbf{r}_i) \end{aligned} \tag{2.1}$$

Here, ϕ_{k-1} represents a k-body interatomic potential, F^{ext} an external force, θ_{ijk} represents the angle between atoms i, j, k connected by bonds and ∇_i is the gradient operator, $\frac{\partial}{\partial x_i}\hat{\mathbf{x}} + \frac{\partial}{\partial y_i}\hat{\mathbf{y}} + \frac{\partial}{\partial z_i}\hat{\mathbf{z}}$. In the present formulation, external forces include those enforcing simulation constraints, such as keeping the wall atoms stationary.

The interatomic potentials can, in simple cases, be derived ab-initio, including from Density Functional Theory (DFT) calculations. In most cases, they are empirically determined such that they reproduce a number of equilibrium or non-equilbrium system properties or benchmark results.

The trajectories generated by the time integration described above correspond to a sequence of system microstates. Assuming ergodicity, these microstates can be sampled to obtain thermodynamic quantities and system properties at equilibrium as well as steady state. In time-evolving systems, averaging in time smears the time-evolution and is not recommended, unless it takes place over time intervals that are much shorter than the characteristic evolution time. In systems where the latter is not possible, averaging over an ensemble of (parallel) calculations needs to be performed.

2.2 MD Simulations for nanoscale tribology

The computational cost of MD simulations scales linearly with the number of timesteps and at best linearly with the number of particles. MD simulations are certainly not feasible alternatives to continuum models whenever the latter are available, since numerical solvers for pdes operate at a high degree of coarse graining when compared to a full atomistic simulation and are hence cheaper. For example, MD simulations [53] of micron-sized cubes of simple fluids require weeks of computational time on powerful supercomputers, because, conversely, MD simulations operate at a much finer level of resolution.

In the context of liquid film lubrication, MD simulation studies are typically warranted for systems with sizes $\lesssim 50\ nm$, where deviations from continuum models based on the Navier-Stokes equations have been observed. However, currently only systems with sizes $\lesssim 10\ nm$ can be simulated without using supercomputing facilities. This is because increasing the characteristic lengthscale of a system, h, increases the simulation cost very quickly; in addition to increasing the number of particles, a larger system lengthscale also icreases the characteristic system timescale (that is proportional to the number of timesteps that need to be simulated) by (approxi-

mately) h^2/η, where η is the fluid kinematic viscosity. Although here we have used a Navier-Stokes scaling for the characteristic timescale, this is justified since we are most concerned about the *largest* system that one can simulate.

2.3 Simulation potentials and program

In this section we discuss the interatomic potentials chosen to model the interactions between different types of atoms, common to all our simulations. We also describe briefly the program used to perform all our simulations.

2.3.1 Interatomic potentials

The EAM (Embedded Atom Method) potential for crystalline Iron [74] was used to model solids throughout this thesis. According to the embedded atom model, the potential energy of atom i, U_i, has two contributions: pairwise interactions and the energy required to place an electron into an electron cloud of local density ρ_i, given by [1, 74]:

$$U_i = \sum_{j \neq i} \phi_{ij}(r_{ij}) + F(\rho_i) \tag{2.2}$$

where, $F(\rho_i)$ is a functional of the local electron density. The latter is constructed such that it reproduces crystallographic data (lattice parameters at different temperatures, BCC $\leftrightarrow$ FCC transition energies, elastic constants, vacancy forming energies and so on) and first principles atomic forces as closely as possible. In the present work, we use "potential 2" fitted by Mendelev et al., that is available in tabular form (version December 2010) at [31].

The liquid lubricant studied in this thesis, n-hexadecane, is modelled using the Transferrable Potentials for Phase Equilibria - United Atom (TraPPE-UA) developed by Martin et al. [72]. This force field predicts the vapor-liquid coexistence curves reliably for n-alkanes and small branched alkanes. In the TraPPE-UA description, each CH_2 and each CH_3 segment of the alkane are considered to be individual *pseudo-*

atoms. Pseudo-atoms separated by more than 3 bonds or atoms which are non-bonded (e.g. belonging to different molecules), interact via the Lennard-Jones(LJ) potential [63]:

$$U_{ij} = 4\epsilon_{AB}\left(\left(\frac{\sigma_{AB}}{r_{ij}}\right)^{12} - \left(\frac{\sigma_{AB}}{r_{ij}}\right)^{6} \right) \tag{2.3}$$

where ϵ_{AB} is the potential well depth and σ_{AB} is the characteristic lengthscale of the interaction (the approximate distance at which repulsion balances attraction) associated with atoms of type A and B. The LJ parameters used in this thesis for both types of pseudo-atoms are given in Table 2.1. The LJ parameters of interaction between atoms of unlike types were calculated using the Lorentz-Berthelot mixing rules:

$$\begin{aligned} \sigma_{AB} &= \frac{\sigma_{AA} + \sigma_{BB}}{2} \\ \epsilon_{AB} &= \sqrt{\epsilon_{AA}\epsilon_{BB}} \end{aligned} \tag{2.4}$$

The following rules apply to pseudo-atoms connected by 3 bonds or fewer. Bond stretching is modelled via a harmonic potential of the form, $U_{ij} = \frac{k_r}{2}(r_{ij} - r_0)^2$, where $r_0 = 1.54\text{Å}$ is the equilibrium bond length and k_r, the bond stretching parameter taken here to have the value 19.5139 $eV/\text{Å}^2$ (chosen from Lopez-Lemus et al [68]). The bending of the angle between 3 adjacent atoms connected through bonds is modelled through a harmonic potential [72] of the form $U_{bending} = \frac{k_\theta}{2}(\theta - \theta_0)^2$, where the bending parameter k_θ is taken as 2.6925 eV and the equilibrium angle, $\theta_0 = 114$ degrees. The torsional potential that arises due to the bending of the dihedral angle, ϕ, is given by an OPLS style potential [110] : $U_{torsion} = \frac{c_1}{2}(1 + \cos\phi) + \frac{c_2}{2}(1 - \cos(2\phi)) + \frac{c_3}{2}(1 + \cos(3\phi))$. The parameters are taken from Martin et al. [72] to be:

$$c_1 = 0.05774 \quad c_2 = -0.0117524, \quad c_3 = 0.136382$$

Type of pseudo-atom i	Type of pseudo-atom j	σ(Å)	ϵ(eV)
CH_2	CH_2	3.95	0.003964
CH_3	CH_3	3.75	0.008445
CH_3	CH_2	3.85	0.0058
CH_2	Fe	3.1347	0.0108
CH_3	Fe	3.0347	0.0158

Table 2.1: The LJ parameters of interaction between different atomic species used in this thesis.

The interactions between the solid and the liquid atoms are computed through an LJ potential (Equation 2.3), using parameters computed through the Lorentz-Berthelot mixing rules in Equation 2.4.

The parameters for the wall-fluid interactions reported in Table 2.1 were calculated using $\epsilon_{FeFe} = 0.02947\ eV$ and $\sigma_{FeFe} = 2.2$ Å, as recommeded by Zheng [115]. Note that these parameters are different from those reported in the literature for BCC Fe (see Zhen et al. [114], for example). They were used by Berro et al. [7] in the simulation of the more realistic Fe oxide surfaces.

2.4 LAMMPS

We performed our simulations using the popular, open-source MD package `LAMMPS` (Large-scale Atomic/Molecular Massively Parallel Simulator) [87, 86]. As suggested by its name, `LAMMPS` is optimized to have high parallel efficiency (even for complicated geometries) that scales well even with hundreds of processors. Some of the large simulations in chapter 4 also used a GPU, in addition to the CPU. This was made possible through the GPU package in `LAMMPS` [15, 13, 14] that accelerates the computation of many-body potentials (the EAM potential in our case).

In `LAMMPS`, simulation constraints are specified through `fix` commands. For example, a Langevin thermostat would be specified through a `fix langevin` command; wall atoms can be kept at a constant velocity by setting the force on them to 0, in a particular direction, using the `fix setforce` command. Measurements of various properties are accomplished through `compute` commands; for instance, the tempera-

ture can be computed at a timestep using the `compute temp` command. All of these measurements are easily time-averaged or spatially averaged, or both, as intended, and output to files.

Most functionalities needed in MD simulation have been abstracted into easy-to-use commands provided by the standard implementation of `LAMMPS` or one of the various packages written by users. This approach has simplified simulations of complex problems (see list of publications page [60]) in various fields of research. Atomic trajectories are visualized using the tool `VMD` (Visual Molecular Dynamics) [48], used extensively in this work. All the `LAMMPS` input files used in the simulations in this thesis are available at [19]. Simple `AWK` and `Julia` scripts used to post-process the outputs generated by LAMMPS are included in [19], for complete reproducibility.

2.5 MD simulations of pressure-driven flow

In this section we outline the simulation methodology and provide input data and parameters for the simulations discussed in chapter 3, where we study the dependence of the flow rate of n-hexadecane in nanoscale channels, Q_p^{MD}, on h, the channel height. We note that the pressure-driven flow is actually generated using the rather standard approach [57] of applying a body force on each fluid atom in the direction of flow. This approach, which exploits the similarity between pressure-driven channel flow and "gravity-driven channel flow" in fully developed settings, simplifies the simulation considerably since the domain can now be periodic in the direction of flow; in contrast, imposing different pressures at each end of the domain would require (large) particle reservoirs at each end and would introduce entrance and exit effects.

2.5.1 Simulation geometry

The simulations are performed in channels of length 99.94 Å in the flow direction, $\hat{\mathbf{x}}$, and width 71.38 Å, in the $\hat{\mathbf{z}}$ directions, as shown in Figure 2-1. The channel width in the transverse $\hat{\mathbf{y}}$ direction, denoted by h, is varied between 1.1 nm and 10.5 nm.

The fluid was bounded by two solid walls in the transverse $\hat{\mathbf{y}}$ direction. Each wall

consists of eight layers of atomically smooth BCC Fe (001) surface, of dimensions 99.94 Å × 71.38 Å × 22.84 Å. In the initial geometry shown in Figure 2-1, the solid slabs are separated by a gap more than the intended h (say, $h + 1$ nm) and the gap is filled with n-hexadecane molecules. The number of molecules is calculated based on the final volume available to the fluid (i.e. for a film thickness of h) and the number density of n-hexadecane at a temperature of 450 K and a pressure of 80 MPa, namely, 0.033Å^{-3} (empirically determined from previous simulations).

Each solid wall consists of two layers of *rigid atoms* on which the force in the shear direction is set to 0 (furthest from the liquid), three *thermostatted* layers of atoms next to the rigid layers on which the NVT thermostat (a thermostatting algorithm that uses Nosé-Hoover-style equations of motion [97, 73, 84], that are time-integrated using an algorithm proposed in [107]) is applied, and three layers (closest to the liquid) that are *deformable*. No constraints are imposed on the *deformable* layers. This model is designed to mimic the long range elastic response of the solid without resorting to using very thick walls that increase the computational cost of the system.

2.5.2 Simulation method

The simulation consists of an initial equilibration followed by application of the body force ("gravity"). During both these steps:

- A uniform force of -0.00083 $\hat{\mathbf{y}}$ $eV/\text{Å}$ is applied to each of the 4375 atoms comprising the rigid layer of the upper wall. This force is the equivalent of 80 MPa of mechanical pressure acting on the fluid; at steady state, when the wall is no longer moving in the $\hat{\mathbf{y}}$ direction, the fluid (thermodynamic) pressure can be approximated by this value.

- An NVT thermostat [97, 107, 73, 84] at a temperature of 450 K is applied on the thermostatted layers of both the upper and lower walls. The damping constant that determines how fast the oscillations in the temperature and volume of the group of atoms are damped out, is taken to be 0.1 ps^{-1}.

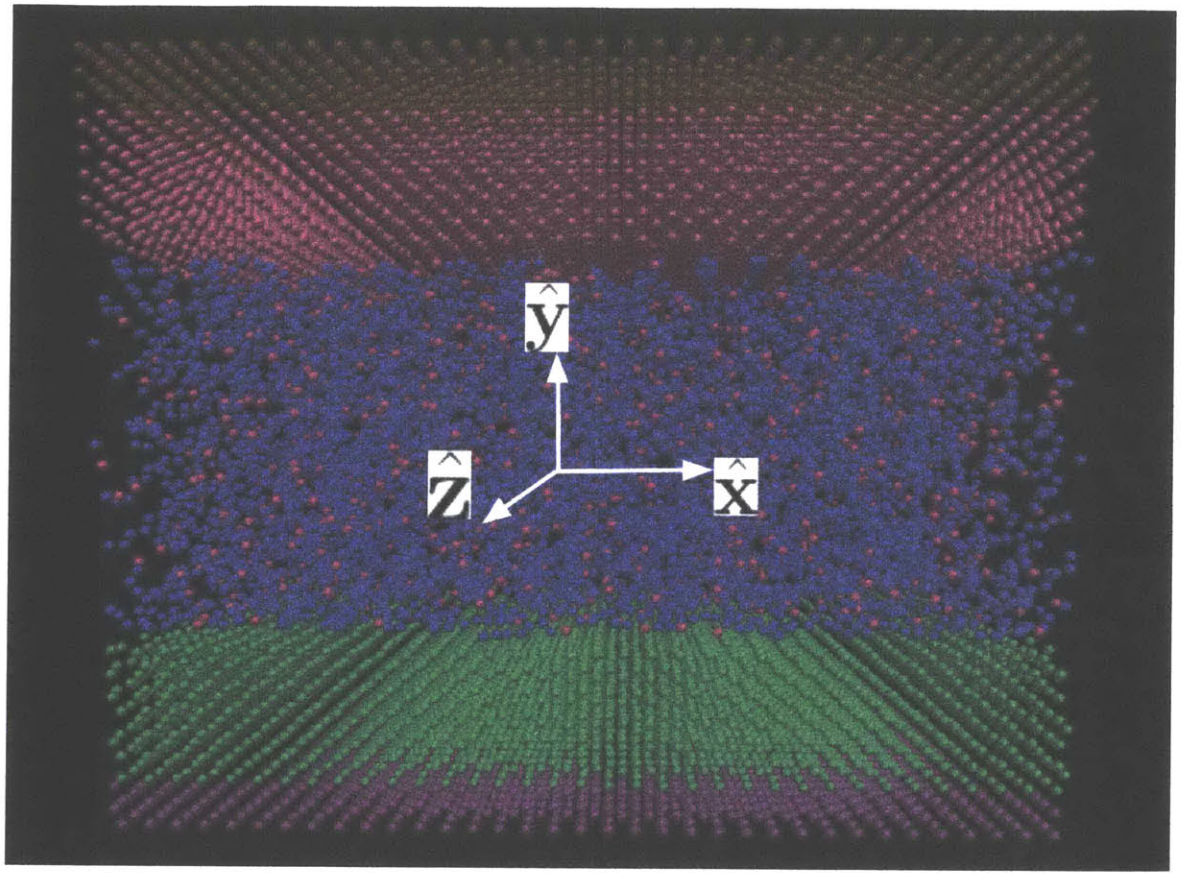

Figure 2-1: The simulation geometry used for Poiseuille flow of n-hexadecane between solid walls. $\hat{\mathbf{z}}$ is the lateral direction pointing out of the plane of the figure. Magenta atoms at the bottom and the brown atoms at the top represent the rigid layers in the lower and upper slabs respectively.

- The rigid layers of the lower wall are held at a fixed y coordinate. The forces on the rigid atoms in both walls are set to 0 in the shear direction, $\hat{\mathbf{x}}$.

- The integration timestep is 2 fs.

Equilibration and thermostatting method

Since the simulation is started at a lower density, the normal force causes the upper wall to descend and undergo damped oscillations until a steady film thickness is achieved. The equilibration is run at a timestep of 2 fs for $1 - 2$ ns (1 ns for the smaller film thickness up to 4 nm and 2 ns, for all film thicknesses greater than 4 nm).

We find that using the Langevin thermostat during the non-equilibrium shear process introduces errors into the velocity profile even if the total force exerted by the thermostat on the center of mass of the liquid atoms is explicitly set to zero at every timestep. Additionally, the thermostat produces artificial changes to the velocity profiles even if

- The drag term and the random term act only on the thermal velocities of the liquid molecules.

- The Langevin thermostat acts upon the velocities only in the $\hat{\mathbf{z}}$ direction (perpendicular to the plane of shear).

There is considerable evidence [98] that thermostatting during shear has an effect on the slip length observed at high shear rates. A thorough discussion can be found in [83], where it is also shown that applying a Langevin thermostat on the liquid during shear produces an unphysical divergence in the slip lengths at high shear rates. As a result of the above observations, once equilibrium is achieved, the Langevin thermostat is turned off in the liquid. The viscous heating produced in the liquid is instead removed by the Nosé-Hoover thermostat applied on the thermostatted wall layers (after being conducted by the fluid to the walls). Removing heat through the walls, as opposed to thermostatting the fluid directly, makes our results more reliable

and also makes our simulation seem a closer replica of laboratory experiments. We have verified that temperature profile remains constant in the $\hat{\mathbf{y}}$ direction, except for some temperature oscillations within a distance of 4 Å from the walls associated with the fluid layering discussed in section 3.1.

Gravity force

In order to simulate a pressure driven flow along the channel axis, a force is applied on all liquid atoms in the direction $\hat{\mathbf{x}}$. The force exerted on each atom is the same and denoted by f. We note that the resulting accelerations $g = f/m$ are many orders of magnitude (up to $10^{12} - 10^{13}$ times) larger than the acceleration due to gravity on earth; this is necessary due to the very small channel height, which requires very large pressure gradients in order to produce flow velocities that are appreciably large compared to the statistical uncertainty associated with the sampling process; this is further discussed below. The magnitude of the force, f, is chosen with the following considerations in mind:

- The temperature of the fluid due to viscous heat generation should not increase significantly. We have empirically determined that fluid velocities up to $\sim$ 50 m/s, do not lead to significant temperature rises.

- The velocity of the fluid needs to be large enough to minimize the sampling time required to achieve an acceptable signal-to-noise ratio. The ratio of the average fluid velocity to its standard deviation is proportional to the product of the Mach number of the flow and the square root of the number of fluid particles present in each bin [41]. Therefore, for a fixed number of simulated molecules, it is advantageous to increase the flow velocities as much as possible while ensuring that the flow remains incompressible. We have empirically determined that maximum flow velocities in the range 20-70 m/s do not introduce compressibility effects and provide good signal-to-noise ratios.

- The shear rate, $\dot{\gamma}$, remains low enough for the slip length to be independent of the shear rate. Several published works have indicated that the slip length in

simple polymeric fluids exhibits a non-linear response captured by:

$$L_s = L_s^0\left(1 - \dot{\gamma}/\gamma_c\right)^{-1/2}$$

where, L_s^0 is the slip length at the zero shear rate limit and γ_c is the critical shear rate beyond which there is no additional interfacial momentum transfer [89, 81, 11, 83]. In this work, we induce shear rates ($\sim \rho g h/2\mu$) in the range 10^9–$10^{10} s^{-1}$ across simulations of different film thicknesses. Although numerically close to the critical value of shear rate mentioned in [89] ($5 \times 10^{-3} \times \sqrt{\frac{\epsilon}{m\sigma^2}}$, where σ and ϵ are LJ parameters of the liquid), our shear rates do not influence the value of the slip length: the slip lengths calculated over a wide range of film thicknesses (shear rates) are nearly constant.

Given the above considerations, f needs to be chosen by also keeping in mind that the body force should be reduced as the film thickness increases in order to maintain comparable shear rates and velocities across the simulations at different film thicknesses. For instance, a force per atom of 10^{-4} $eV/\text{Å}$ and 1.5×10^{-5} $eV/\text{Å}$ were applied on the liquid atoms in the simulation where the film thickness was 1.6 nm and 9 nm respectively; the maximum velocities attained in the respective simulations were 21.6 m/s and 26.2 m/s.

Data collection method and run times

Ultimately, the quantity of interest that we wish to obtain from these simulations is the pressure-driven flow rate, Q_p^{MD}. This flow rate is easily calculated from the velocity profile obtained from MD. In order to obtain the velocity profile, the liquid volume is divided into cuboidal bins of size $L_x \times y_{bin} \times L_z$, where y_{bin} is chosen to be 1Å here. Note that the bins span the entire simulation box in both the $\hat{\mathbf{x}}$ and $\hat{\mathbf{z}}$ directions. The flow rate is obtained from:

$$Q_p^{MD} = \sum_k \frac{1}{N_t} \sum_t u_k(t)$$

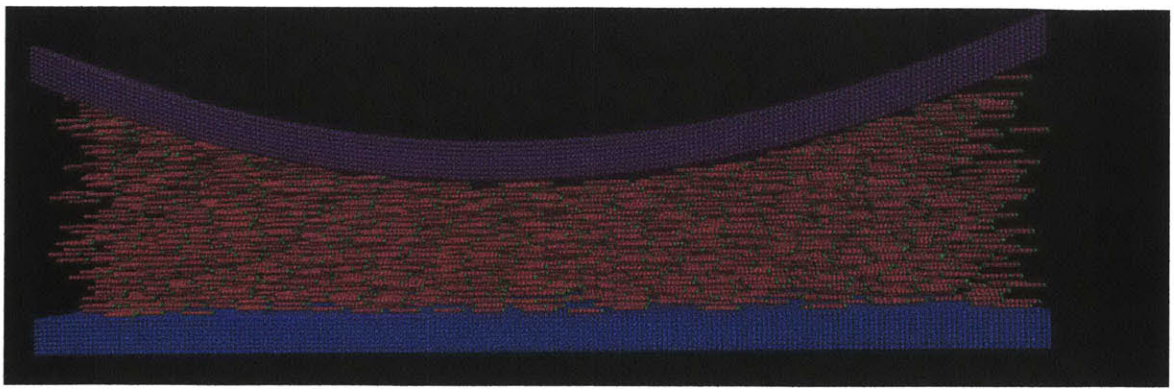

Figure 2-2: MD simulation box geometry for the barrel-drop model. The walls are BCC Fe and the liquid consists of n-hexadecane molecules. The coordinate system used is the same as in Figure 2-1 and the rest of this thesis.

where $u_k(t)$ is the center of mass velocity of the fluid in the kth bin at the timestep t (after a steady-state has been reached) and N_t is the number of timesteps sampled.

Sampling of molecular data begins 2 ns after the start of the application of the gravity force. This time is significantly longer than the time needed to reach steady state, estimated as h^2/η and typically expected to be on the order of a few picoseconds. Molecular velocities are sampled every timestep. Simulation run times for flow vary between 5 ns for the smallest film thickness to 20 ns for the largest. The standard error in the time average of the velocities was at least an order of magnitude smaller than the mean itself.

2.6 MD simulation of the barrel-drop problem

MD simulations of the barrel-drop geometry were performed for validating the new lubrication description, the MODEL, developed in chapter 3. The validation is performed by comparing the lubricant pressure distribution obtained from MD simulation with the same quantity as predicted by the MODEL.

The geometry of the barrel-drop profile is shown in Figure 2-2. A parabolic ring surface is created with BCC Fe atoms; the lower wall is smooth, as in the Poiseuille flow simulations. Both the upper parabolic surface and the lower plane surface consist of rigid, thermostat and deformable layers, with analogous constraints

to those discussed in the previous section on Poiseuille flow. The coordinate system used is the same as in the Poiseuille flow simulations (shown in Figure 2-1) and that used throughout this thesis. Periodic boundary conditions are imposed in the shear direction, $\hat{\mathbf{x}}$ and the homogeneous (depth) direction, $\hat{\mathbf{z}}$. The extent of the simulation box in the $\hat{\mathbf{x}}$ direction is $L_x = 599.62$ Å and the simulation box size in the $\hat{\mathbf{z}}$ direction is $L_z = 256.97$ Å. The minimum film thickness is $h_0 = 3.8\ nm$, while the maximum film thickness is 7.8 nm. The total number of liquid molecules is 15815. The total number of Fe atoms is 585900.

The simulation is initialized by filling the gap with fluid molecules with a slightly lower number density than expected at a temperature of 450 K and a pressure of 80 MPa. The system is then equilibrated under an applied load in the $\hat{\mathbf{y}}$ direction equivalent to a pressure of 80 MPa The equilibration phase is taken to have a duration of 2 ns, after which a steady film thickness is observed. The walls do not undergo a measurable deviation from their parabolic shape as a result of the equilibration or the shearing process.

The thermostatting procedures during equilibrium are identical to the Poiseuille flow simulations and as described in section 2.5.2. The temperature of the fluid is maintained by a Langevin thermostat at 450 K during the equilibration stage. The solid is maintained at 450 K through an NVT thermostat applied to the thermostatted layers throughout the simulation (both during equilibrium and during shear). The timestep used is 2 fs.

After equilibration, the fluid thermostat is turned off and the lower wall starts to move (in the $-\hat{\mathbf{x}}$ direction) with a constant speed $U = 60\ m/s$. The normal load remains applied, maintaining the applied system pressure at 80 MPa.

The viscous heating produced in the liquid is dissipated through the thermostatted layers in the solid. As a result, during the non-equilibrium phase of the simulation we see an average temperature of 447 K in the liquid, with a maximum fluctuation of $\pm 10K$.

After an additional time of 2 ns, (1×10^6 steps with a timestep of 2 fs), the pressure in the liquid film is averaged for the next 3 ns. This is accomplished in `LAMMPS` with a

combination of the `compute chunk/atom` and `compute ave/chunk` commands. The simulation box in divided into cuboidal bins of dimensions 3 $nm \times 4\ nm \times Lz$. The pressure in each bin is calculated as the average over time of one third of the trace of the stress tensor [101]. In `LAMMPS`, the stress tensor is computed using the `compute stress/atom` command, which returns the product of the stress tensor of an atom and its volume computed from Voronoi tesselations. Therefore, to obtain the stress tensor within a bin the contributions of all atoms within each bin need to summed and divided by the volume occupied by the fluid atoms of that bin.

Chapter 3

Molecular Dynamics-based Equation for Lubrication

MD simulation has been very succesful in providing physical insight into transport at the nanoscale and has been employed extensively by researchers studying boundary lubrication problems (some examples include [115, 7, 94, 116]). On the other hand, a continuum formulation of boundary lubrication remains very desirable for a number of reasons: first, it will be less expensive to solve numerically than MD simulations; second, it will enable modelling of macroscopic problems that involve boundary lubrication at some location (or many locations) of the physical domain; third, it can provide physical insight at the lubrication level that is more accessible to practitioners.

In this chapter we demonstrate the development of such a continuum description based on a modified Lubrication Equation that is valid even at an atomistic lengthscale.

3.1 Background

In this section we provide some background discussion of the main theoretical ingredients of the proposed approach: lubrication theory and slip-flow theory. While the former is a standard analysis tool in the field of IC engines, the need for invoking

slip-flow theory has not received significant attention in this field.

The most remarkable finding, perhaps, from the many studies concerned with microscale/nanoscale fluid flow and transport is that the Navier-Stokes description is remarkably robust [33, 40]. Specifically, the general consensus is that the stress-strain constitutive relation remains valid well below the micrometer scale and even as the nanoscale is approached. As characteristic confinement lengthscales decrease, deviations from the no-slip Navier-Stokes behavior typically appear first at the liquid-solid boundaries, in the form of slip [6]. In fact, slip is always present at the boundary between a liquid and a solid. However, as will become more apparent below, its contribution becomes non-negligible as the characteristic flow lengthscale becomes small, typically within an order of magnitude of the fluid characteristic lengthscale (mean free path for a gas and characteristic molecular size for a liquid). This explains why the no-slip boundary condition has been succesful in describing macroscopic fluid dynamics and slip boundary conditions need only be considered in small-scale flows. Further discussion follows in subsection 3.1.2 and subsection 3.1.3.

3.1.1 The lubrication approximation

Let us begin by considering an incompressible liquid lubricant film bounded by solid surfaces of infinite extent in the lateral directions, $\hat{\mathbf{x}}$ and $\hat{\mathbf{z}}$, perpendicular to the direction of the fluid film thickness, $\hat{\mathbf{y}}$, as shown in Figure 3-1. We start by reviewing the assumptions that underlie classical lubrication theory (see [62, 16] for a detailed description), while noting that these assumptions remain applicable to a large class of problems and even at the nanometer length scales that we study in this thesis. In the interest of simplicity, we will limit the discussion to flows of the type depicted in figure 3-1, in which no flow exists in the $\hat{\mathbf{z}}$ direction (also $\partial/\partial z = 0$) and only the lower boundary moves in the negative $\hat{\mathbf{x}}$ direction with speed U, while the gap height is characterized by $h = h(x)$. (Here we note that a lower case letter refers to the coordinate along the respective direction denoted by capped letter. We also note that the fluid velocity vector $\mathbf{u}$ has components u, v and w along the $\hat{\mathbf{x}}$, $\hat{\mathbf{y}}$ and $\hat{\mathbf{z}}$ directions).

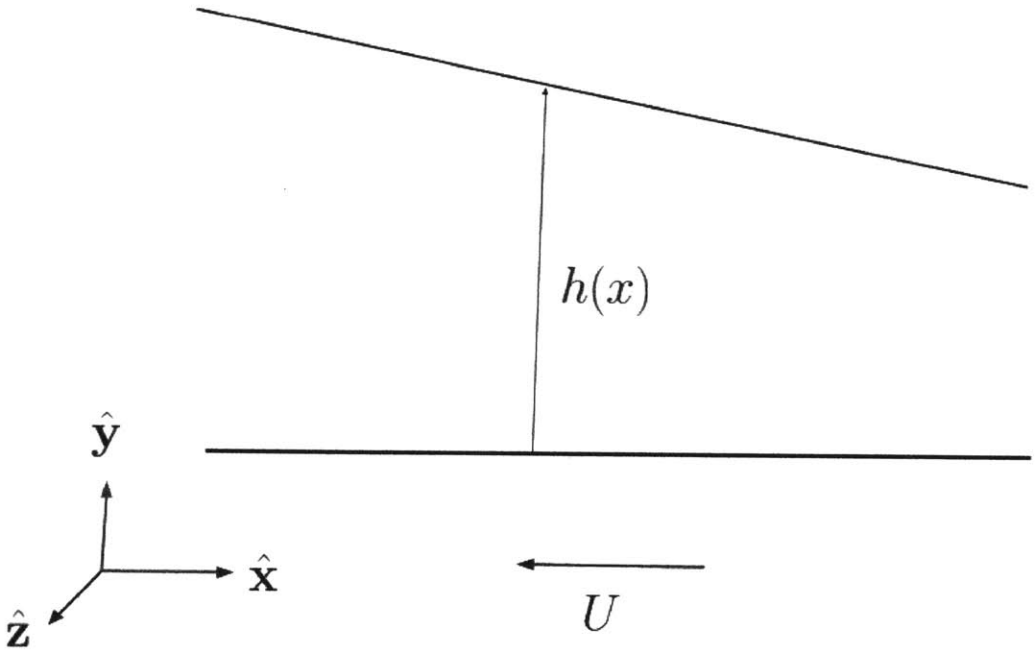

Figure 3-1: Sketch of a typical lubrication analysis geometry.

- The ratio of the characteristic length scale, h_0, in the transverse direction, $\hat{\mathbf{y}}$, to the characteristic length scale, L, in the axial direction $\hat{\mathbf{x}}$, denoted by $\epsilon = h_0/L$, is small, i.e., $\epsilon \ll 1$. In our MD simulations of lubricated gaps, we typically have $\epsilon \sim \mathcal{O}(0.1)$. For the oil flow between the Twin-Land Oil Control Ring (TLOCR) and the cylinder liner, considered in chapter 5, $\epsilon \sim \mathcal{O}(10^{-3})$.

- Lubricant flows are characterized by a low Reynolds number and therefore it is safe to assume that $\epsilon^2 Re \ll 1$. In other words, narrow-gap flows are dominantly driven by viscous forces and pressure gradients as opposed to inertial forces. The largest contribution to the viscous force comes from $\mu\, \partial^2 u/\partial y^2$, since the gradient of the axial velocity $u = u(x, y, z)$, in the y and z directions is negligible, $\mathcal{O}(\epsilon)$. Viscous forces are balanced by the pressure gradient term, $\dfrac{\partial p}{\partial x}$. The fluid film thickness is also assumed to vary slowly in the lateral directions, $|\dfrac{\partial h}{\partial x}| \ll 1$. While this assumption doesn't seem manifest in the Reynolds equation, it reminds us that rapid changes in the flow rate are unphysical.

- We also note that the requirement $\epsilon^2 Re \ll 1$ ensures that the time-dependent inertia terms ($\dfrac{\partial u}{\partial t}$, $\dfrac{\partial v}{\partial t}$, $\dfrac{\partial w}{\partial t}$), are negligible. This condition can be rewritten in the form,

$$\frac{h_0^2}{L^2}\,\frac{U_0 L}{\eta} \ll 1,$$

  where U_0 is the characteristic speed which implies $h_0^2 U_0/(\eta L) \ll 1$ or $h_0^2/\eta \ll T$, where $T = L/U_0$. In other words, the characteristic time scale, T, is much larger than time scale for viscous diffusion across the lubrication gap, h^2/η. For example, in a typical piston ring-liner lubrication problem, we have, $h^2/(\eta T) \sim 10^{-5}$, where T is the time period of a piston stroke [20]. This means that the magnitude of the inertial force is negligible in comparison to the viscous term.

Under these simplifying assumptions, the incompressible Navier-Stokes equation for a one-dimensional isothermal, pressure-driven flow reduces to

$$\frac{\partial p}{\partial x} = \mu \frac{\partial^2 u}{\partial y^2} \tag{3.1}$$

For isothermal problems, this equation can be integrated along with the continuity equation given appropriate boundary conditions. Fortunately, the geometry associated with these flows lends itself to a significantly more convenient description in which the continuity equation is already automatically incorporated, known as the Reynolds equation. This is briefly discussed below.

The Reynolds lubrication equation

Integrating the continuity equation for an incompressible fluid over the film thickness we obtain

$$\int_0^{h(x)} \frac{\partial v}{\partial y} dy = -\int_0^{h(x)} \frac{\partial u}{\partial x} dy = -\frac{\partial}{\partial x}\int_0^{h(x)} u dy + \frac{\partial h}{\partial x} u(y = h(x))$$

$$\implies v(y = h(x)) - v(y = 0) = -\frac{\partial}{\partial x}\int_0^{h(x)} u dy + \frac{\partial h}{\partial x} u(y = h(x)) \tag{3.2}$$

Using the impermeability constraint at the lower wall [18], (in our setting) $v(y = 0) = 0$. In the presence of slip, the impermeability condition at the upper wall at $y = h$ is

$$\frac{\partial h}{\partial t} = v(y = h) - \frac{\partial h}{\partial x} u(y = h(x)).$$

Thus, we obtain

$$v(y = h(x)) - \frac{\partial h}{\partial x} u(y = h(x)) = \frac{\partial h}{\partial t} = -\frac{\partial}{\partial x}\int_0^{h(x)} u dy$$

or

$$\frac{\partial h}{\partial t} + \frac{\partial Q}{\partial x} = 0 \tag{3.3}$$

where

$$Q = \int_0^{h(x)} u dy$$

is the (local) volumetric flow rate.

This formulation is very convenient because the above equation already incorpo-

rates mass conservation, but also because it reduces the Navier-Stokes problem that needs to be solved to that of unidirectional flow in a local film of thickness h, that is, essentially channel flow. We refer to the flow rate obtained for the simple case of pressure-driven flow between stationary walls, as Q_p, where the subscript p stands for Poiseuille flow (for historic reasons). We use Q_c to denote the flow rate obtained between walls moving with constant velocity, with no pressure gradients, where c stands for Couette flow. In any isothermal flow, the flow rate, Q, can be split into its Couette flow and Poiseuille flow contributions [35], ie, $Q = Q_c + Q_p$. We refer to the corresponding flow rates in Poiseuille and Couette flow obtained when we assume no slip at the boundaries as Q_p^{NS} and Q_c^{NS} respectively. We obtain $Q_p^{NS} = -\dfrac{h^3}{12\mu}\dfrac{dp}{dx}$ and $Q_c^{NS} = -\dfrac{Uh}{2}$, with the no slip boundary conditions for Poiseuille and Couette flows respectively. The classical Reynolds equation thus becomes

$$\frac{\partial h}{\partial t} = \frac{\partial}{\partial x}\left(\frac{h^3}{12\mu}\frac{dp}{dx} + \frac{Uh}{2}\right) \tag{3.4}$$

We will now discuss slip boundary conditions and subsequently arrive at expressions for Q_p and Q_c.

3.1.2 Slip in dilute gases

We begin our discussion of slip (arising due to small-scale confinement) with the case of dilute gases, in which, the weak interaction between molecules makes theoretical analysis easier. In dilute gases, slip-flow theory is a well-established branch of rarefied gas dynamics; the interested reader is refered to [40] for a discussion of the origins of *slip flow theory* and its application in the continuum modelling of kinetic effects, as described by the Boltzmann equation.

Summarizing the main result of slip-flow theory, for a gas in contact with a solid boundary moving with velocity U, the velocity of the gas at the boundary is given by

$$u|_w - U = \alpha\,\lambda \left.\frac{\partial u}{\partial y}\right|_w \tag{3.5}$$

where $|_w$ denotes the boundary (wall) location, y the wall normal pointing into the gas, λ is the mean free path and α is a constant that depends on the gas-wall interaction [40].

We note that the relation in Equation 3.5 can be *derived* by a rigorous asymptotic analysis of the Boltzmann equation and coefficient α numerically calculated to many significant digits [99]. Efficient simulation methods for dilute gases (such as the Direct Simulation Monte Carlo (DSMC)) have also been invaluable for the validation of these results (e.g., see [2] for comparison of DSMC solutions with slip flow NS solutions of flow fields in gas lubricated bearings).

3.1.3 Slip in dense fluids

Unfortunately, due to the strong interactions between molecules in a fluid, the dense fluid case is significantly more complex and no well established theoretical framework for its study exists. As a result, slip in dense fluids is treated mostly approximately and, depending on the system of interest, sometimes empirically. The most widely used slip-flow description, known as the Navier boundary condition,

$$u|_w - U = L_s \left.\frac{\partial u}{\partial y}\right|_w \tag{3.6}$$

comes from the simplistic assumption of linear response at the wall. It resembles the first order model for rarefied gaseous flows stated in Equation 3.5, but substitutes the known slip coefficient $\alpha\lambda$ with an empirical slip coefficient, L_s, known as the slip length.

Although originally proposed without any microscopic considerations in mind, it can be justified microscopically by introducing the wall-fluid friction coefficient, β, as proportionality coefficient in

$$\tau_{xy}|_w = \beta(u|_w - U) \tag{3.7}$$

relating the wall shear stress to the slip velocity at the wall, in a linear response sense

[104, 11, 5]. If the Newtonian stress-strain constitutive relationship also holds, i.e.

$$\tau_{xy}|_w = \mu \left. \frac{\partial u}{\partial y} \right|_w , \tag{3.8}$$

we obtain the Navier slip boundary condition, Equation 3.6, by combining the assumptions in Equation 3.7 and Equation 3.8 and interpreting the slip coefficient as the ratio of the viscosity to the friction coefficient

$$L_s = \frac{\mu}{\beta}.$$

The slip length, L_s, is usually on the order of nanometers and is hence insignificant in larger fluid systems, although the phenomenon of slip at the solid surface exists at all length scales. The wall-fluid friction coefficient is closely related to the fact that at small scales, fluids near solid walls exist in layers (see [37, 90, 61] for early MD simulations that confirmed this fact). There is rich literature (see [91, 49] for a review) available that qualitatively discusses the correlation between various parameters such as the corrugation in the wall potential, wall attraction, surface roughness, film thickness, applied load, temperature, etc, with the layering phenomena in a static fluid as well as during flow. Rigorous understanding of the layering and the in-plane structure in these layers that are of utmost importance to micro- and nano- tribology is yet to be achieved.

Barrat and Bocquet [11, 5] provided a starting point with an approximate expression for the slip length derived using Green-Kubo theory to calculate the friction coefficient, β. Their expression reads

$$L_s \approx \frac{(k_B T)^2}{S(q_0)\sigma \int_0^\infty \rho(y) V_{FS}(y)^2 \, dy} \tag{3.9}$$

where $S(q_0)$ is the fluid structure factor evaluated at the first wave vector of the solid substrate's reciprocal lattice, q_0. In the above expression, σ refers to the molecular diameter, $\rho(y)$ represents the fluid density profile in the thickness direction and V_{FS} is the wall-fluid interaction potential. This expression is expository in many ways:

- It establishes the slip boundary condition as a phenomenological relationship, arising from interfacial friction, at the atomic level. It is consistent with our intuition about the fluid-solid momentum transfer at the interface:
  - As the surface binding energy increases, the slip decreases as expected. The slip length, as per [103], is inversely proportional to the integral of the surface potential term that increases with increasing fluid-philicity of the surface. This behavior has been confirmed both experimentally [24] and via MD simulations [113].
  - As the commensurability between the ordering in the fluid adjacent to the solid layers and the solid increases, we expect the interfacial momentum transfer to increase, which results in smaller slip. The structure factor term precisely describes this relationship and it has been confirmed in [113] that the relationship between L_s and $(S(q_0)\rho(h))^{-1}$ collapses into a straight line even at shear rates of $\sim 10^{11}\ s^{-1}$.
- We observe in our Poiseuille flow simulations discussed later that the slip length varies significantly with temperature. An increase in temperature of $10K$ to a system consisting of C-16 lubricant between atomically smooth Fe substrates maintained at 447 K, causes a 10% increase in the slip length observed. The dependence on pressure is expressed both through the integral term (that is proportional to the fluid density near the wall) and the structure factor term. At high pressures, the effect of fluid layering near the walls becomes significant and $S(q_0)$ larger, which leads to a decrease in the slip length [6] .

3.1.4 The effect of slip on the lubrication equation

In a Couette flow, it is readily seen that the presence of slip introduces symmetric deviations from the no-slip flow profile, leaving the overall flow rate the same as the no-slip Couette flowrate, that is, $Q_c = Q_c^{NS} = Uh/2$ for the Couette flow shown in Figure 3-4. The overall flow rate in a Poiseuille flow, Q_p, on the other hand, is altered in the presence of slip. Applying the Navier slip condition Equation 3.6 to the two

boundaries, namely at $y = 0$ and $y = h$,

$$\begin{aligned} u(0) &= L_s \frac{\partial u}{\partial y}\Big|_{y=0} \\ -u(h) &= L_s \frac{\partial u}{\partial y}\Big|_{y=h} \end{aligned} \tag{3.10}$$

we obtain

$$u(y) = \frac{1}{2\mu}\frac{dp}{dx}\Big(y^2 - (y + L_s)h\Big). \tag{3.11}$$

and thus

$$Q_p = \int_0^{h(x)} u(y)\, dy = -\frac{1}{\mu}\frac{dp}{dx}\Big(\frac{h^3}{12} + \frac{L_s h^2}{2}\Big) \tag{3.12}$$

We see that the correction term to the no-slip solution is $\mathcal{O}(L_s h^2)$ and this explains why slip is negligible for $h \gg L_s$. This correction term increases the flow rate (compared to no slip) for a given driving force and gap height, as would be expected, since the flow velocity is not reduced to zero at the wall. As will be seen in chapter 4 and chapter 5, the consequence of this "reduction in effective flow resistance" is to lower peak pressures in lubrication problems.

Substituting the expressions for Q_c and Q_p into the mass conservation equation in Equation 3.3, we have the following Reynolds equation modified to include slip corrections:

$$\frac{\partial h}{\partial t} = \frac{\partial}{\partial x}\left(\frac{1}{\mu}\frac{dp}{dx}\Big(\frac{h^3}{12} + \frac{L_s h^2}{2}\Big) + \frac{Uh}{2}\right) \tag{3.13}$$

3.2 The limits of Navier-Stokes theory and Navier slip-flow relation

The development of a framework for describing lubrication flows at small scales starts by first understanding the limitations of the currently prevalent description (i.e. the Navier-Stokes-based lubrication equation 3.4) and its origin.

Using an analogy from rarefied gas dynamics [40], one expects deviations from Navier-Stokes behavior to appear when the gap height is on the order of, or less than, ten times the characteristic molecular size. This argument is more clear when dealing with simple (e.g. Lennard-Jones) fluids for which the molecular (atomic) size is clearly defined. When considering complex fluids, including long-chain polymeric fluids, the characteristic molecular size is not well defined, since it is also affected by the confinement. For this reason, we performed Poiseuille flow simulations of the model lubricant studied in this thesis (n-hexadecane) between smooth Fe walls for several film thicknesses in the range 1-11 nm. With these simulations we hope to identify precisely the extent to which the Navier-Stokes description and Navier slip condition can be used in the lubrication equation; moreover, we expect that the MD simulations will allow us to extract a value for L_s for the modeled system. The MD simulation methodology is discused in detail in section 2.5.

3.2.1 The limits of Navier-Stokes theory

Figure 3-3 shows the velocity profiles obtained from simulations at many different film thicknesses, normalized by the maximum velocities observed in each simulation. The velocity profiles were found to be parabolic when the film thickness was $\gtrsim 4.5\ nm$. This indicates that the NS equation is robust in films consisting of a mere ~ 10 atomic layers. More specifically, obtaining a parabolic profile affirms that the linear relationship between the shear stress and strain rate used in deriving the NS equation, is valid even in ultra-thin films of thicknesses $\sim 4.5\ nm$.

Note that obtaining a parabolic velocity profile may be a sufficient indication of

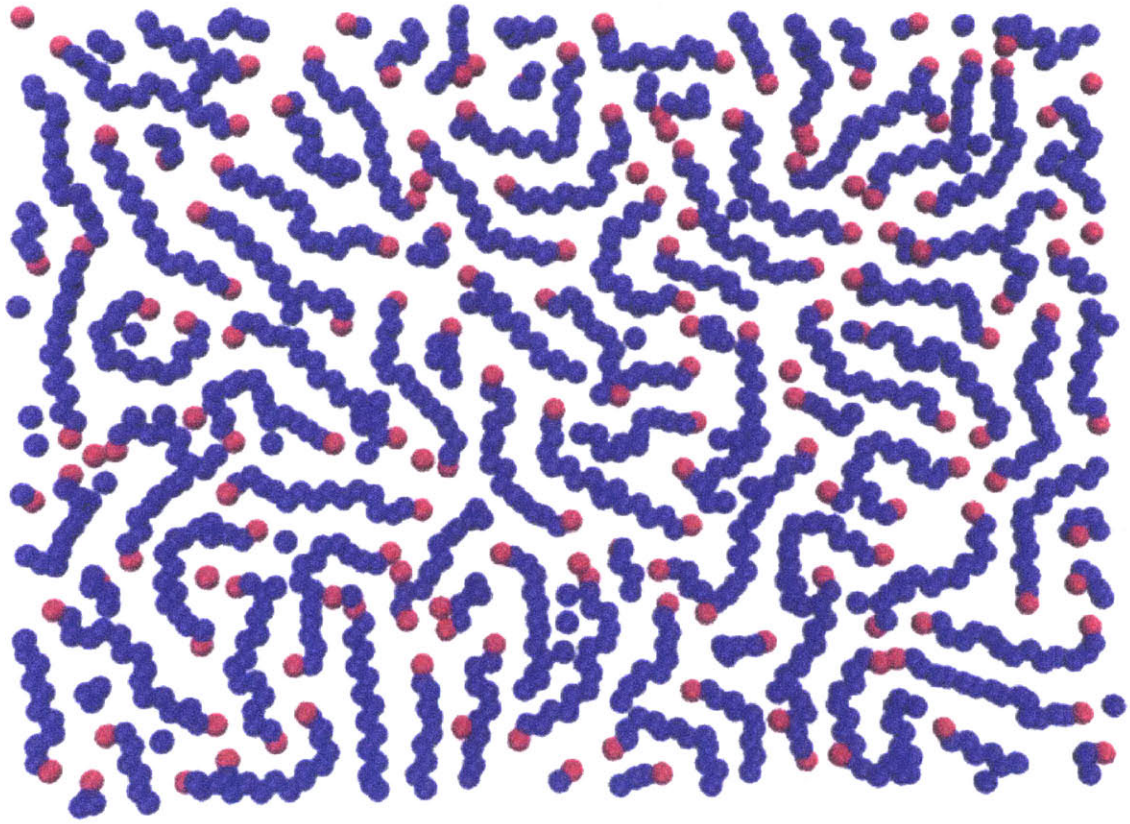

Figure 3-2: The fluid structure in the $\hat{\mathbf{x}} - \hat{\mathbf{z}}$ plane, during shear, in the first layer adjacent to the stationary wall. Under the high shear rates employed, the nonequilibrium states of the fluid still show high in-plane ordering, as well as layering, that are not significantly different from that observed at equilibrium [10]. This suggests that the Green-Kubo relationship for the slip length derived by Barrat and Bocquet [11, 5] could still be applicable in our simulations.

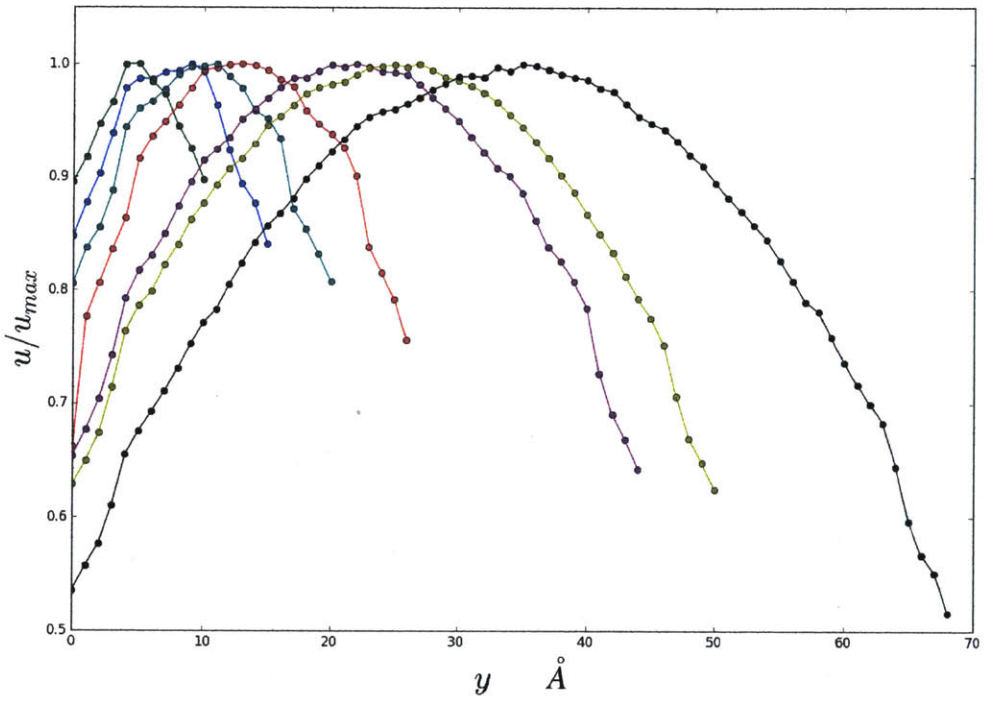

Figure 3-3: The velocity profiles along the thickness direction, $\hat{\mathbf{y}}$, obtained from Poiseuille flow simulations for films of various thicknesses in the range $1 - 11$ nm. The velocities are scaled by the maximum velocity observed in each simulation.

the validity of a constitutive relation of the form Equation 3.8 at that film thickness; however, it does not imply that Navier-Stokes theory is valid, since for this to be true, the coefficient of viscosity in the constitutive relation 3.8 should be independent of the film thickness (as a material property). Indeed, for *nearly* parabolic films with thicknesses in the range $3.2\ nm \leq h \leq 4.5\ nm$, we do observe "viscosity" values that deviate by about 50% at the same temperature when compared to the values of the viscosity calculated from the bulk fluid (of thickness greater than 10 nm). On the other hand, we observe that the coefficient of viscosity calculated from the velocity profiles are all within 10% of 0.5 $mPas$ for all the simulated thicknesses in the range 4.5 - 10.5 nm. For even smaller film thicknesses, $\leq\sim 3.2\ nm$, the velocity profiles, as can be seen from Figure 3-3, are not parabolic and hence the "coefficient of viscosity" values cannot be extracted from Poiseuille flow simulations.

We also observe the same trend in the viscosity values (and approximately the same limits for Navier-Stokes behavior) in Couette flow simulations, using the standard method of obtaining the viscosity coefficient by dividing the shear stress by the apparent velocity gradient (see [10] for example). At the same temperature and applied pressure as the Poiseuille flow simulations, we obtain viscosity values computed from $\mu = \tau_{xy}/(\frac{\partial u}{\partial y})$, for a film thickness of 4.6 nm to be within 5% of the value 0.5 $mPa\ s$, in agreement with those obtained from Poiseuille flow simulations. The velocity profiles obtained in the Couette flow simulations at different sliding speeds of a 4.6 nm thick film, are shown in Figure 3-4. In Couette flow simulations at smaller film thicknesses, the values of the coefficients of viscosity obtained from simulations are highly thickness-dependent. Deviations observed in the coefficient of viscosity from the value of 0.5 $mPa\ s$, are in the range $25 - 50\%$ for films of thickness between $1.7 - 3.9\ nm$. This is related to the fact that the quantities such as the *coefficient of viscosity* and the *slip length* that arise in constitutive relationships that rely on the continuum assumption lose physical relevance when the fluid volume entirely consists of ordered layers. In this scenario, wall-effects dominate the behavior of the fluid since the *bulk* volume is negligible.

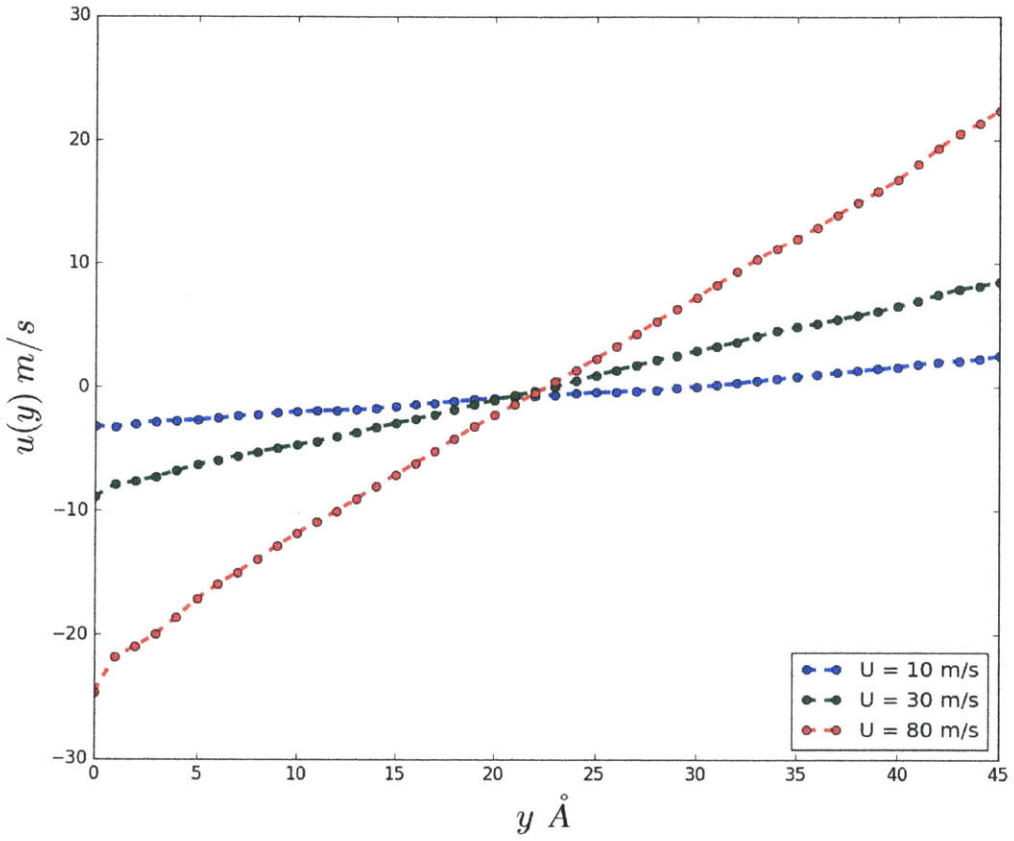

Figure 3-4: The velocity profiles obtained in Couette flow simulations of an n-hexadecane film of thickness 4.6 nm. The velocity of the upper wall is set at $U/2\ \hat{\mathbf{x}}$ and the lower wall is set at $-U/2\ \hat{\mathbf{x}}$, where U, the relative velocity of the upper wall wrt the lower wall, is as shown in the legend. For all these different shear rates, the value of the coefficient of viscosity was consistently found to be $\sim 0.5\ mPas$.

3.2.2 The limits of the Navier slip boundary condition

After having analyzed the limits of applicability of the NS assumption, we similarly gauge the extent of validity of the other constitutive equation that we used in deriving Equation 3.13, namely the slip relationship Equation 3.6.

The slip lengths computed from the parabolic velocity profiles obtained in the Poiseuille flow simulations of thicknesses in the range $h \gtrsim 5\ nm$ are consistently within 10% of 2 nm. These values are also clearly impervious to the changes in the shear rate in the range of shear rates $10^9 - 10^{10}\ s^{-1}$.

For film thicknesses that are beyond the limits of Navier-Stokes validity as defined in the previous subsection (i.e. smaller than about 4.5 nm), one does not anticipate that the Navier slip boundary condition Equation 3.6 will be reliable. Even if Equation 3.7 holds true, Equation 3.6 is not expected to hold (in fact, our MD simulations of Couette flow for gap heights in the range $17 - 46$ Å show that β exhibits a weak dependence on film thickness), since the coefficient of viscosity depends on the film thickness and thus L_s depends on the film thickness. For thinner films, the layering at the wall becomes severe and leads to behavior that has yet to be fully characterized.

One also has to consider whether a slip relation, of any form in fact, is useful, if the constitutive relation Equation 3.8 is not valid: the slip relation serves as a boundary condition for the solution of the Navier-Stokes; when the latter fails a boundary condition for the axial velocity field is no longer necessarily valuable. Moreover, numerous previous studies have analyzed the tendency of the strong layering phenomenon to induce solid-like behaviors in the fluid [61, 49, 37, 90].

3.3 Lubrication equation for arbitrary lengthscales

The central takeaway from the MD results is that *the Newtonian constitutive relationship Equation 3.8 and the Navier slip boundary condition Equation 3.6 fail for ultrathin films.* If one insists on defining a *coefficient of viscosity* and a *slip length* at those lengthscales, those appear to deviate from their values in *bulk films* and also exhibit non-trivial dependences on spatial location and the gap height.

The limits of applicability of these constitutive relationships can be approximately determined from MD simulations as described above. These limits are themselves functions of the simulation conditions, the wall fluid interaction and, of course, the precise definition of "Navier-Stokes failure" (how much error can be tolerated?).

Is it possible to extend continuum (lubrication equation) modelling to this ultrathin film regime where deviations from Navier-Stokes behavior are not negligible? The remainder of the present chapter is devoted to a formulation that makes this possible. The basic idea behind this formulation is that although Equation 3.4 assumes Navier-Stokes behavior, removing the assumption of a Navier-Stokes-based flow rate, that is returning to Equation 3.3, gives a mass conservation equation that is valid at all lengthscales. In other words, provided Equation 3.3 is "closed" with a model for Q that is valid beyond the Navier-Stokes description, the resulting lubrication equation should also be valid beyond the Navier-Stokes description. Here we note that this approach has already been used in dilute gases (see [35, 36, 77] for example) where solution of Boltzmann equation leads to accurate and reliable expressions for Q beyond the Navier-Stokes description. In what follows we develop such a description for Q and thus a lubrication equation that is valid beyond the Navier-Stokes description.

3.4 Lubrication flow rates beyond the Navier-Stokes description

In subsection 3.1.4 we had derived expressions for the Poiseuille and Couette flow components Q_p and Q_c respectively, of the total flow rate in a slip corrected Reynolds equation. In this section, we derive functional forms of the flow rate components that are approximations to the true flow rates obtained from Molecular Dynamics simulations in order to derive the Molecular Dynamics-based Equation for Lubrication (MODEL).

For reasons that will be more clear later, we will focus our attention on the

Poiseuille component of the flow rate, which we write in the general form

$$Q_p^{MODEL} = \tilde{Q}(h, p, B)\frac{dp}{dx}, \tag{3.14}$$

where p denotes the pressure and B the particular liquid-boundary interaction considered (Note that the flows we consider are all isothermal so the effect of temperature is neglected). One might expect that $\tilde{Q} \propto h^n$, with $1 \leq n \leq 3$, since $n = 3$ for Navier-Stokes with no-slip (and thus $\tilde{Q} \propto h^3$ as $h \gg L_s$), while $n = 1$ appears to be a resonable lower bound, since the flow rate is expected to be proportional to the width of the gap.

In principle, the functional form $\tilde{Q}$ can be obtained from MD simulations or experiments. Here we use the former. In fact, we use the observation that Q_p given in Equation 3.12 would be an accurate starting point for Q_p^{MODEL} since, as we have shown in the previous section, $Q_p^{MD} \rightarrow Q_p$ for $h \gtrsim 4.5 \;\; nm$, where Q_p^{MD} is the Poiseuille flow rate obtained from MD simulations. We therefore propose

$$Q_p^{MODEL} = Q_p \times F(h, L_s, B), \tag{3.15}$$

where $F(h, L_s, B)$ is a function that asymptotically tends to 1 as the film thickness increases.

Perhaps surprisingly, our simulation results, shown in Figure 3-5, suggest that choosing $F = 1 \; \forall h$, results in a good fit to the flow rate data obtained from MD simulations. Here we note that the slip length and viscosity in Q_p^{MODEL} were computed to be

$$\begin{aligned} L_s^* &= 2.1 \; nm \\ \mu^* &= 0.54 \; mPa \; s \end{aligned} \tag{3.16}$$

from a least squares fit of Q_p to the MD data (Q_p^{MD}) for film thicknesses greater than 5.8 nm.

In other words,

$$Q_p^{MODEL} = -\frac{dp}{dx}\left(\frac{h^3}{12\mu^*} + \frac{L_s^* h^2}{2\mu^*}\right) \tag{3.17}$$

We have not paid much attention to the Couette contribution to the MODEL flow rate, Q_c^{MODEL}, because it, rather conveniently remains the same as the no-slip Navier-Stokes result, namely $Uh/2$. This can be readily seen from symmetry arguments, but has also been extensively validated by molecular dynamics simulations [51, 50] that show increasing slip at smaller lengthscales, but, of course, a profile that is always symmetric about the average velocity of the two walls. In other words, the Molecular Dynamics-based Equation for Lubrication (MODEL) is given by:

$$\frac{\partial h}{\partial t} = \frac{\partial}{\partial x}\left(\frac{dp}{dx}\left(\frac{h^3}{12\mu^*} + \frac{L_s^* h^2}{2\mu^*}\right) + \frac{Uh}{2}\right) \tag{3.18}$$

3.4.1 Velocity profile comparison

The most surprising result, perhaps, of this thesis, is the observation that the slip-corrected Poiseuille flow rate, Q_p, continues to describe the flow rate for $h \lesssim 4.5\ nm$, where the *slip-corrected* Navier-Stokes description is considered invalid. In this section we give more evidence that this is a fortuitous result, most likely related to the particular fluid-solid system considered here. In the previous section we have noted that for $3.2\ nm \lesssim h \lesssim 4.5\ nm$ the coefficient of viscosity extracted from approximately parabolic profiles was film-thickness (h) dependent, while for $h \lesssim 3.2\ nm$, the velocity profiles were not parabolic. This is shown more clearly in Figure 3-6 which shows the velocity profiles observed in the MD simulation at 4 different film thicknesses and compares those to the predictions of Equation 3.11, derived earlier in this chapter, using the parameters obtained in Equation 3.16. Clearly, the Navier-Stokes profiles become better approximations to the *true* profiles obtained from MD as the

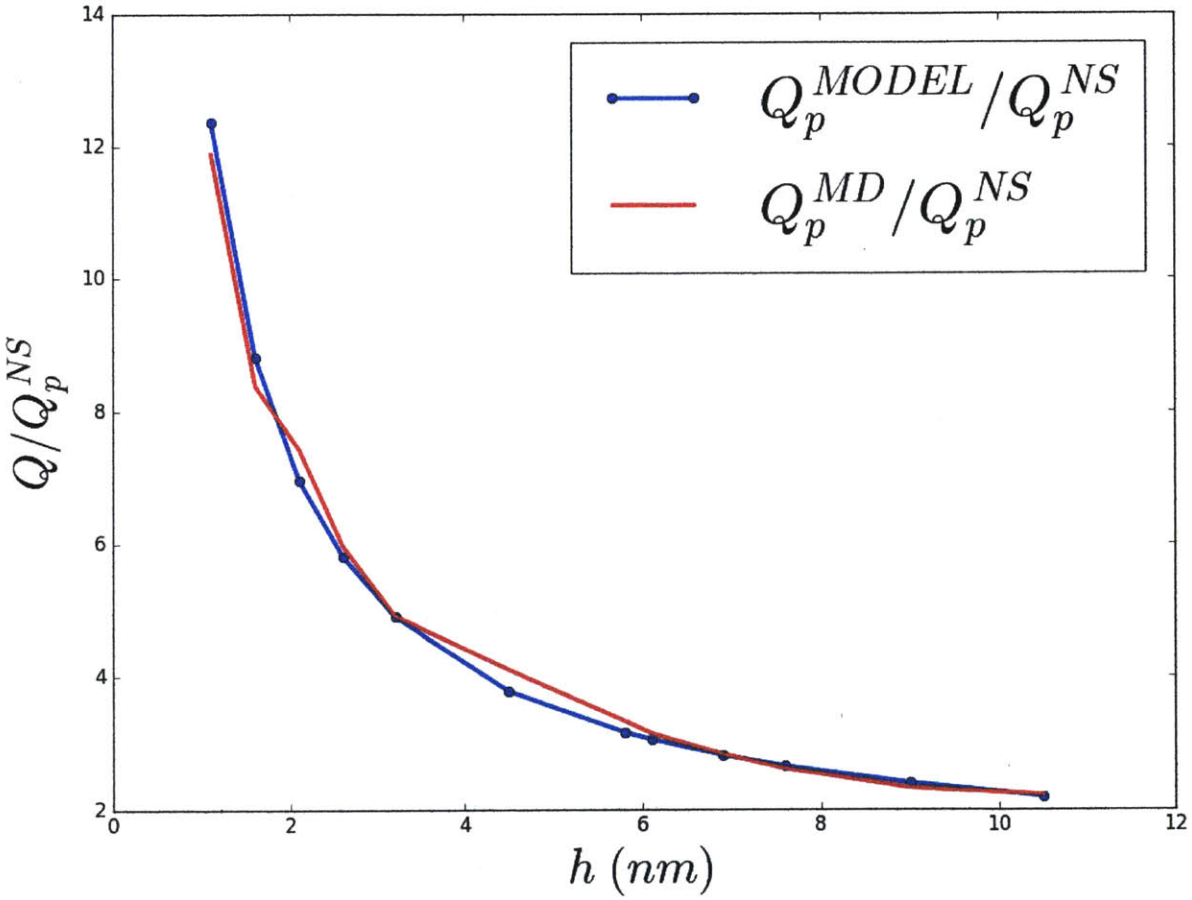

Figure 3-5: Comparison between Q_p^{MODEL} given by Equation 3.17 and MD results for the flow rate, Q_p^{MD}, for 1.1 $nm \leq h \leq 10.5$ nm.

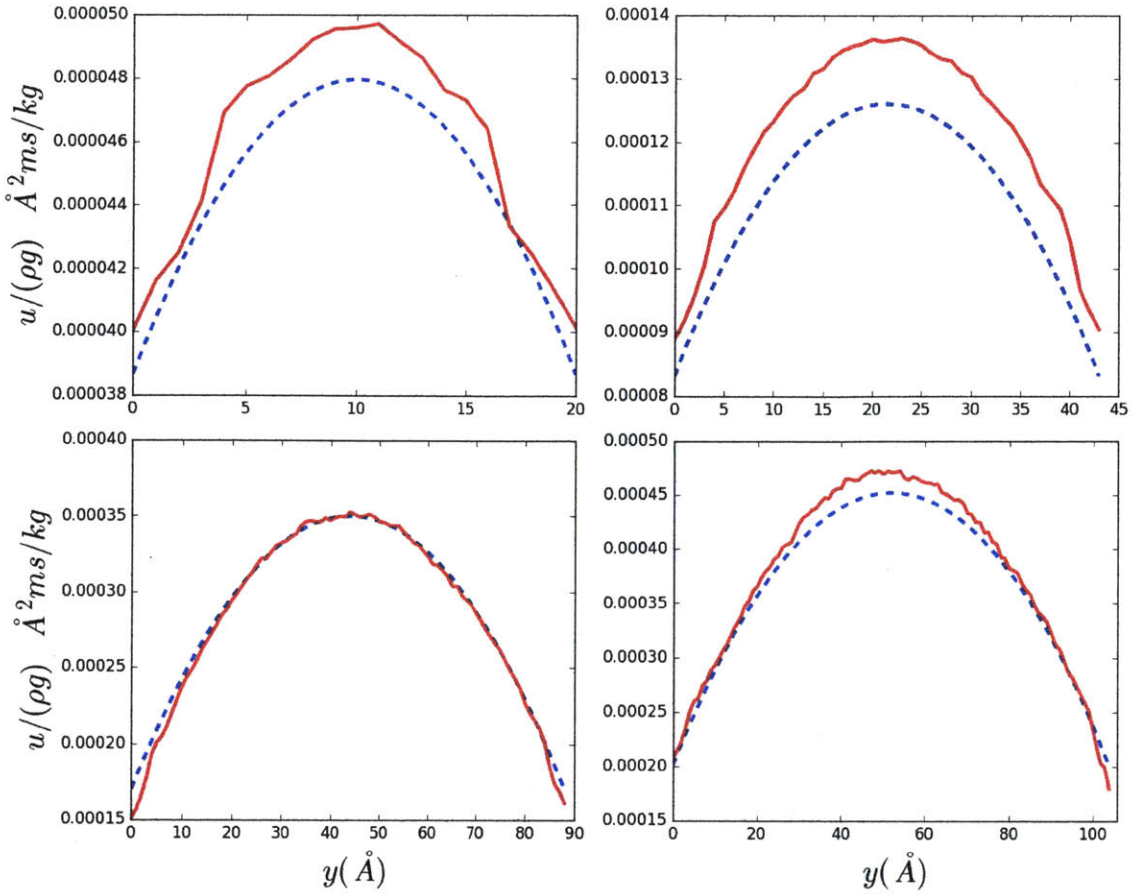

Figure 3-6: Velocity profiles Equation 3.11 for films of thickness $h = 2\ nm, 4.4\ nm, 8.9\ nm$ and $10.5\ nm$. The blue curves denote solutions of slip-corrected Navier-Stokes with parameters given in Equation 3.16 while the red curves are those obtained from the MD simulations.

film thickness increases.

At the same time, the flow rate continues to be described well by Q_p. This is seen more clearly in Figure 3-7 which shows the ratio of the MD flow rates, Q_p^{MD} to Q_p^{MODEL} (the latter is the same as Q_p with parameters given in Equation 3.16). For the small film thicknesses of interest here ($h \lesssim 4.5\ nm$), the relative error is small (smaller than for $h \sim 5.8\ nm$ which was used to fit the data) despite the fact that due to the increasing importance of slip, the flow rate in absolute terms is one order of magnitude larger than the flow rate predicted by Navier-Stokes with no slip (see Figure 3-5).

We finally note that the comparison in figures 3-5 and 3-7 is limited to $h > 1.1\ nm$

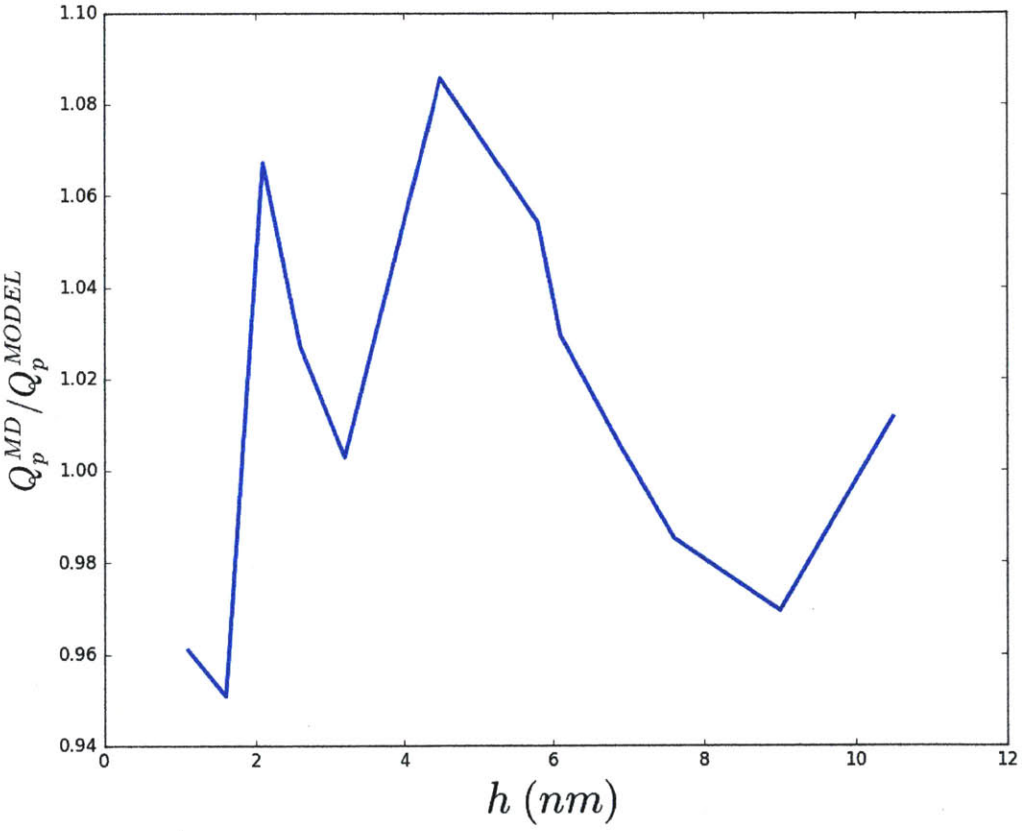

Figure 3-7: Ratio of MD flow rates to Q_p^{MODEL}.

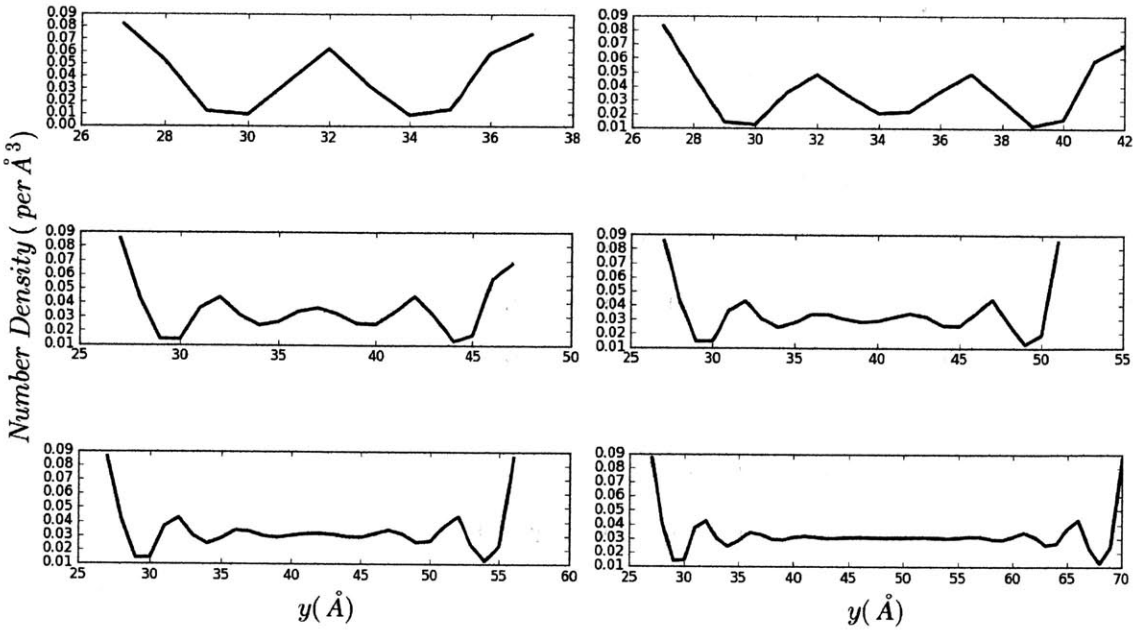

Figure 3-8: The density profile observed at different film thicknesses. The oscillations in the density are correlated with the layering of the fluid normal to the walls.

due to the intense layering observed as the film becomes so small, that makes quantitative analysis in terms of continuum concepts (density, velocity, pressure, etc.) very difficult. This is demonstrated in Figure 3-8 which shows that as the film thickness decreases the atomic layering observed at the boundaries becomes the dominant factor affecting the local density in the film [37, 61].

3.5 Conclusions

In this chapter we analyzed the limits of the Navier-Stokes constitutive law (Equation 3.8) and the Navier slip condition (Equation 3.6). We note that in this work we have adopted a rather severe definition of validity limits; in particular, behavior obeying the same constitutive relation but with a viscosity/slip coefficient dependent on the film thickness have not been considered to be indicative of Navier-Stokes validity. Despite this, we find that the Navier-Stokes description is remarkably robust, making accurate predictions of velocity profiles in ultrathin films with thicknesses as small as $\sim 4.5\ nm$. Because the Navier slip condition makes use of the constitutive

law Equation 3.8 to connect the wall shear stress to the velocity gradient at the wall, it is considered here to fail at the same lengthscale as the Navier-Stokes description.

The main contribution of this chapter is the development of a general lubrication equation that can be used even at lengthscales for which the Navier-Stokes description is not valid. This more general description, referred to as the MODEL, is based on the fact that mass conservation, which is the basis for the classical Reynolds equation, is valid at all length scales. Therefore, when coupled with a constitutive relation for the flow rate that is valid beyond Navier-Stokes, it can be used to describe lubrication problems beyond the realm of Navier-Stokes modelling.

Surprisingly, we find that for the lubricant n-hexadecane bounded by smooth Iron walls, the Navier-Stokes equation with slip and viscosity parameters computed from MD provide an excellent fit to the observed MD data for films as thin as just 3 atomic layers. At these lengthscales, the flow rate is significantly larger than that predicted by Navier-Stokes theory without slip. However, the slip corrected flow rate relation Q_p appears to describe the flow rate measured in MD simulations to within 10 percent with no other correction needed, even though the slip-corrected Navier-Stokes description does not describe the velocity profiles well.

The proposed MODEL is validated in the following chapter by comparing a MODEL solution with MD simulation results for an example lubrication problem. In chapter 5, we analyze the effect of incorporating slip effects at even larger scales, under mixed/hydrodynamic lubrication in a real IC engine environment.

Chapter 4

Ring-Liner Friction Using Slip-Corrected Reynolds Equation

In this chapter and the next we explore the effect of slip phenomena on the hydrodynamics of the lubrication layer between the piston rings and the cylinder liner in IC engines. We begin by studying analytically the difference in the estimated load bearing capacity and the friction between the slip-corrected and the no-slip solution to the Navier-Stokes equation, using a simplified model of the piston ring-liner interface. Using the simplified ring-liner geometry, we validate the MODEL concept and particular closure for the fluid-wall system developed in chapter 3 by comparing the analytical solution for the pressure computed from the MODEL against MD simulations of the same geometry.

4.1 Simplified model of piston ring-liner gap

Consider the barrel-drop geometry shown in Figure 4-1 and originally discussed in section 2.6, serving as a model for the location of closest approach between the pleateau part of the liner roughness and one of the top two piston rings. The plateau part of the liner roughness tends to have a surface roughness average, $Ra \sim \mathcal{O}(0.1\mu m)$; the ring surface has a roughness that is an order of magnitude smaller than the liner surface and is usually considered smooth in comparison [67, 20]. In the present simple

model we neglect the roughness of both surfaces.

In this model, as shown in Figure 4-1, the lubricant film thickness between the ring surface and the liner thus has a parabolic shape

$$h(x) = h_0 + ax^2 \tag{4.1}$$

We assume that the lubricant is Newtonian and that the flow is incompressible; although the shear rates in the MD simulations are large in absolute terms ($\sim \mathcal{O}(10^9)s^{-1}$), they are still lower than typical values where shear-rate dependence is observed [89, 81]. We also assume that the parabolic surface is rigid and satisfies the lubrication assumption, $\frac{\partial h}{\partial x} \ll 1$.

We now apply lubrication theory to obtain expressions for the frictional and normal force associated with this lubrication flow.

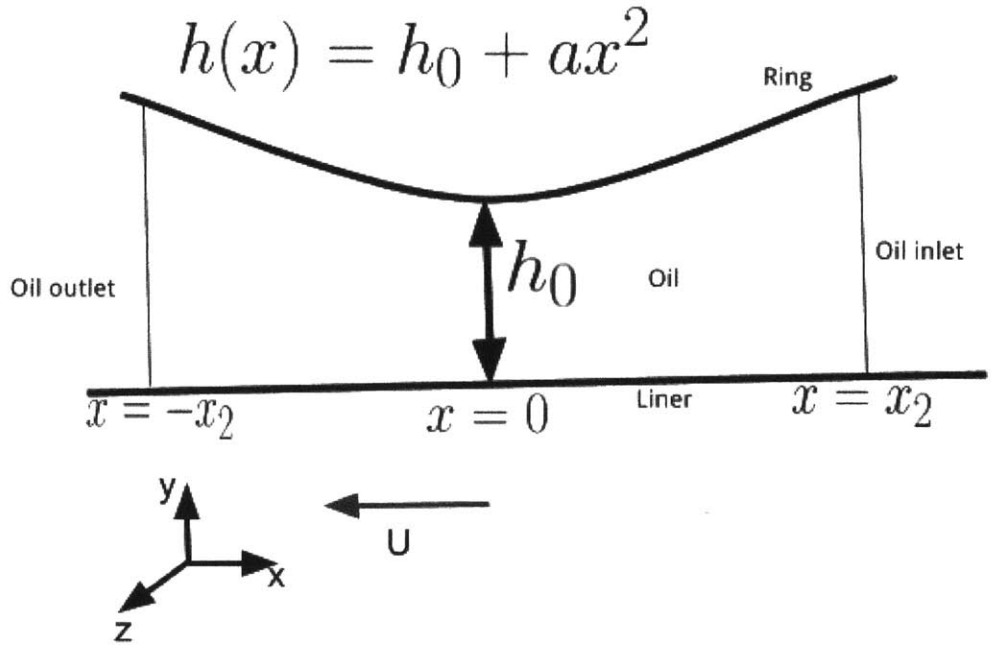

Figure 4-1: Schematic of the lubricated region between the top ring, modelled as a parabolic surface and the liner, modelled as a smooth surface. The notation on the figure refers to the problem formulated in section 4.2.

4.2 Pressure in the fluid film

In the frame of reference attached to the ring, as shown in Figure 4-1, the film thickness at any given x does not change with time. In other words, we have $\partial h/\partial t = 0$. The steady slip-corrected Reynolds equation (see Equation 3.13) reduces to

$$-Q = \frac{1}{\mu}\frac{dp}{dx}\left(\frac{h^3}{12} + \frac{L_s h^2}{2}\right) + \frac{Uh}{2} = \text{const.} \tag{4.2}$$

In this section we consider the boundary condition

$$\left.\frac{dp}{dx}\right|_{x=x_2} = 0 \tag{4.3}$$

where the x_2 is the inlet of the film in the frame of reference of the ring, as shown in Figure 4-1. This assumption automatically implies

$$\left.\frac{dp}{dx}\right|_{x=-x_2} = 0,$$

which is referred to as the Reynolds boundary condition in the tribology literature (see [16, 8] for example). This can be seen by noting that given Equation 4.3, $Q = -Uh(x_2)/2$; considering the flow rate at $x = -x_2$,

$$-Q = \left.\frac{1}{\mu}\frac{dp}{dx}\right|_{x=-x_2}\left(\frac{h(-x_2)^3}{12} + \frac{L_s h(-x_2)^2}{2}\right) + \frac{Uh(-x_2)}{2},$$

we conclude that $\left.\frac{dp}{dx}\right|_{x=-x_2} = 0$ since the film thickness is a symmetric function ($h(x_2) = h(-x_2)$).

The boundary condition (4.3) also requires $p(-x_2) = 0$ in order for continuity in the flow rate to be satisfied. To see this, we consider the point x_0 in the diverging region of the flow ($x_0 \leq 0$, in the frame of reference of the ring) where the pressure reduces below 0 (the ambient pressure in the surrounding fluid) and the fluid film tends to exist as a liquid-vapor mixture. In locations of smaller x, the flow rate

contiunity is maintained by this mixture of vapor and liquid at uniform pressure [16, 20]; that is, $\frac{dp}{dx} = 0 \ \forall \ x \leq x_0$. This point, x_0 is therefore $-x_2$ since $\left.\frac{dp}{dx}\right|_{x=-x_2} = 0$.

On integrating the Reynolds equation with the condition (4.3), we obtain

$$\frac{dp}{dx} = -\frac{\mu U(h - h(x_2))}{2\left(\frac{h^3}{12} + \frac{L_s h^2}{2}\right)} \tag{4.4}$$

$$\implies p(x) - p(-x_2) = p(x) = -\int_{-x_2}^{x} \frac{6\mu U(h - h(x_2))}{\left(h^3 + 6L_s h^2\right)} \, dx \tag{4.5}$$

In the region $-x_2 \leq x \leq x_2$, the pressure gradient is clearly positive and the pressure is increasing. Specifically, we have,

$$p(x_2) = p_{max} = -\int_{-x_2}^{x_2} \frac{6\mu U(h - h(x_2))}{\left(h^3 + 6L_s h^2\right)} \, dx \tag{4.6}$$

If the no-slip boundary conditions had been considered instead, we would have,

$$p_{max}^{NS} = -\int_{-x_2}^{x_2} \frac{6\mu U(h - h(x_2))}{h^3} \, dx \tag{4.7}$$

4.3 Forces on the ring

In this section, we quantify the effect of slip on the forces on the parabolic surface. For a Newtonian fluid, the stress tensor $\mathbf{T}$ at a point (x, y, z), in the fluid, is given by $\mathbf{T} = -p\mathbf{I} + 2\mu\mathbf{D}$, where $\mathbf{D}$ is the strain-rate tensor [100].

Consider a differential surface of area $ds \times dz$ on the ring, with a normal pointing in the direction $\hat{\mathbf{n}}$ as shown in Figure 4-2. The slope of the tangent to the surface is given by $\tan\theta = \frac{\partial h}{\partial x}$. From Figure 4-2 we have, $\hat{\mathbf{s}} \cdot \hat{\mathbf{x}} = \cos\theta, \hat{\mathbf{s}} \cdot \hat{\mathbf{y}} = \sin\theta$, and $\hat{\mathbf{n}} \cdot \hat{\mathbf{x}} = -\sin\theta, \hat{\mathbf{n}} \cdot \hat{\mathbf{y}} = \cos\theta$. The force exerted on the ring at a point (x, y, z) is given by $-\hat{\mathbf{n}} \cdot \mathbf{T} = -\mathbf{t}$ [100]. If F represents the total force on the ring along $\hat{\mathbf{x}}$ and N the

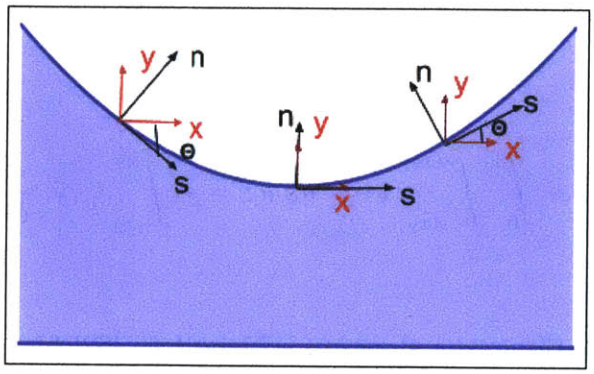

Figure 4-2: Ring-liner interface with the normal and tangential directions indicated by **n** and **s**, respectively.

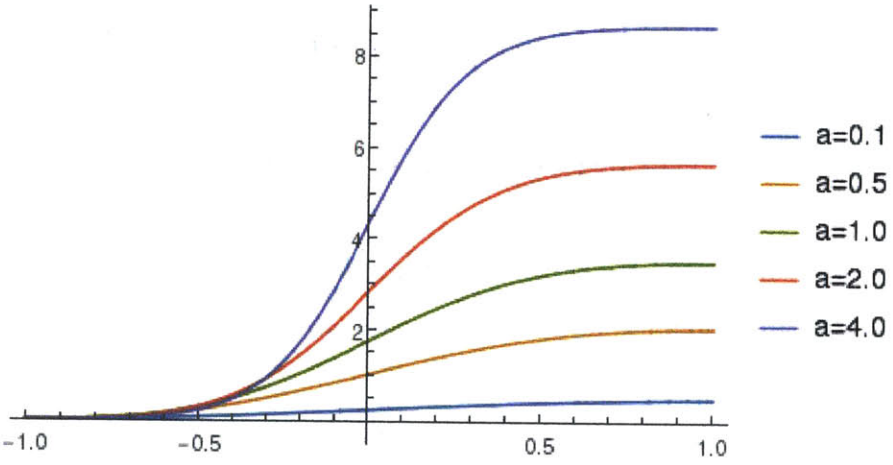

Figure 4-3: Non-dimensional pressure, $\frac{p\epsilon^2 L}{\mu U}$, computed with a slip length $L_s = 0.1h_0$, as a function of the non-dimensionalized x-coordinate, x/L. a in the figure represents the non-dimensionalized parameter of the parabola, aL^2/h_0.

total force along $\hat{\mathbf{y}}$, for a unit width along $\hat{\mathbf{z}}$ (the depth direction), we have,

$$F = -\int_0^1 \int_{-s(x_2)}^{s(x_2)} \mathbf{t} \cdot \hat{\mathbf{x}} \; ds \, dz = -\int_{-x_2}^{x_2} \mathbf{t} \cdot \hat{\mathbf{x}} \; \frac{dx}{\cos\theta} \tag{4.8}$$

and

$$N = -\int_0^1 \int_{-s(x_2)}^{s(x_2)} \mathbf{t} \cdot \hat{\mathbf{y}} \; ds \, dz = -\int_{-x_2}^{x_2} \mathbf{t} \cdot \hat{\mathbf{y}} \; \frac{dx}{\cos\theta}$$

We now use a non-dimensionalization scheme (see [62] for a detailed discussion) that introduces a tacit appreciation of the relative magnitudes of the forces on the ring described above, and in fact, in any general lubrication problem. As discussed earlier, the ratio of the characteristic length scale in the thickness direction (h_0) to that in the lateral directions (L), is given by $\epsilon \ll 1$. The non-dimensional lengths in the different directions are therefore

$$x^* = x/L, \quad y^* = \epsilon y/L, \quad z^* = z/L$$

The characteristic speed along $\hat{\mathbf{x}}$ can be chosen to be U, the relative sliding speed between the ring and the liner. From the continuity equation we conclude [62] that the characteristic speed, v_c, along the thickness direction, $\hat{\mathbf{y}}$, is ϵU.

As emphasized by Leal [62], we can see that the characteristic scale for pressure can be inferred from the characteristic scales fixed so far, namely

$$\begin{aligned} \frac{dp}{dx} &= \mu \frac{\partial^2 u}{\partial y^2} \\ \implies \frac{dp^*}{dx^*}\frac{p_c}{L} &= \frac{\mu U}{h_0^2}\frac{\partial^2 u^*}{\partial y^{*2}} \\ \implies p_c &\sim \mathcal{O}\left(\frac{\mu U}{L\epsilon^2}\right), \end{aligned} \tag{4.9}$$

where the superscript $*$ indicates non-dimensional quantities. Returning to the expressions for the total forces per unit depth (Equation 4.8 and Equation 4.9), we

tion 4.9), we have

$$
\begin{aligned}
F &= -\int_{-x_2}^{x_2} \mathbf{t}\cdot\hat{\mathbf{x}}\frac{dx}{\cos\theta} = -\int_{-x_2}^{x_2}\Big(-\tau_{xx}\sin\theta+\tau_{yx}\cos\theta\Big)\frac{dx}{\cos\theta} \\
&= -\int_{-x_2}^{x_2}\left(-\sin\theta(-p+2\mu\frac{\partial u}{\partial x})+\mu\cos\theta\Big(\frac{\partial u}{\partial y}+\frac{\partial v}{\partial x}\Big)\right)\frac{dx}{\cos\theta} \\
&= -\int_{-x_2}^{x_2}\Big(p\tan\theta+\mu\frac{\partial u}{\partial y}+\mathcal{O}(\epsilon\mu U/L)\Big)\quad\frac{dx}{\cos\theta} \qquad (4.10)\\
&\approx -\int_{-x_2}^{x_2}\Big(p\frac{\partial h}{\partial x}+\mu\frac{\partial u}{\partial y}\Big)\quad dx \qquad (4.11)
\end{aligned}
$$

In going from Equation 4.10 to Equation 4.11, we ignore the terms of $\mathcal{O}(\mu\epsilon U/L)$ since the other terms contributing to the friction are of $\mathcal{O}(\frac{\mu U}{\epsilon L})$. We also use the fact that for the barrel-drop problem, $h(x) = h_0 + ax^2$ and therefore, $\partial h/\partial x = 2ax = \mathcal{O}(\epsilon)$.

Similarly,

$$
\begin{aligned}
N &= -\int_{-x_2}^{x_2}\mathbf{t}\cdot\hat{\mathbf{y}}\frac{dx}{\cos\theta} = -\int_{-x_2}^{x_2}\Big(-\tau_{yx}\sin\theta+\tau_{yy}\cos\theta\Big)\frac{dx}{\cos\theta} \\
&= -\int_{-x_2}^{x_2}\left(-\mu\sin\theta\Big(\frac{\partial u}{\partial y}+\frac{\partial v}{\partial x}\Big)+\cos\theta\Big(-p+2\mu\frac{\partial v}{\partial y}\Big)\right)\frac{dx}{\cos\theta} \\
&= \int_{-x_2}^{x_2}(p+\mathcal{O}(\epsilon\mu U/h))\quad dx \\
&\approx \int_{-x_2}^{x_2} p\ dx \qquad (4.12)
\end{aligned}
$$

The normal force per unit axial length, is clearly of $\mathcal{O}(\frac{\mu U}{\epsilon^2}) \sim \mathcal{O}(F/\epsilon)$; generation of large lifting forces in comparison to shear forces is a well-known feature of fluid films confined under gaps of high aspect ratio.

4.4 Slip effects in the barrel-drop model

In this section we discuss results obtained by numerically integrating relations Equation 4.12 and Equation 4.11, as a means of highlighting the effect of slip on the hydrodynamics of thin-film lubrication. Figure 4-3 shows the pressure distribution

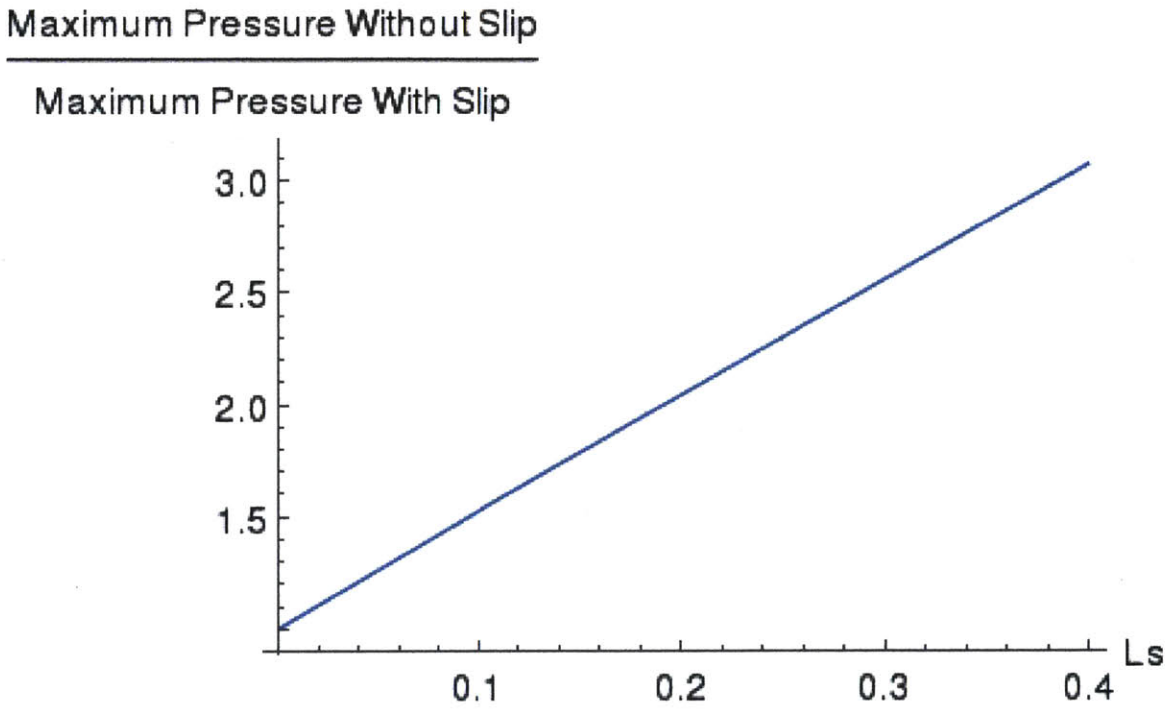

Figure 4-4: Ratio of the pressure calculated from the classical Reynolds equation with no-slip boundary conditions to that computed from the slip-corrected Reynolds equation at $x_2 = 1$, as a function of slip length, in non-dimensional units defined in section 4.3. The plot shows that the overestimation of pressure is significant (~ 1.5 times) even when the minimum film thickness is 10 times the slip length.

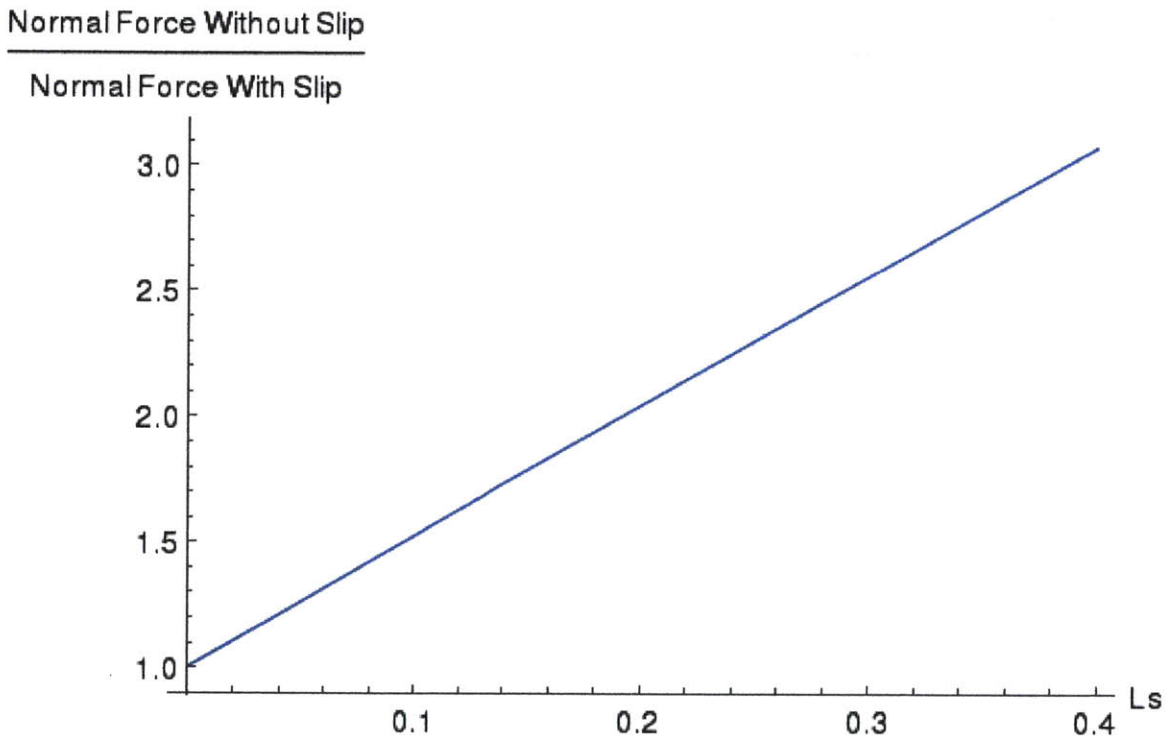

Figure 4-5: Ratio of the normal force calculated from the slip corrected Reynolds equation to the normal force calculated from the classical Reynolds equation with no-slip boundary conditions, at $x_2 = 1$, as a function of slip length, in non-dimensional units defined in section 4.3. The normal forces are calculated by numerically computing the integrals in Equation 4.12. The plot shows that the overestimation of the normal force is significant (~ 1.5 times) even when the minimum film thickness is 10 times the slip length.

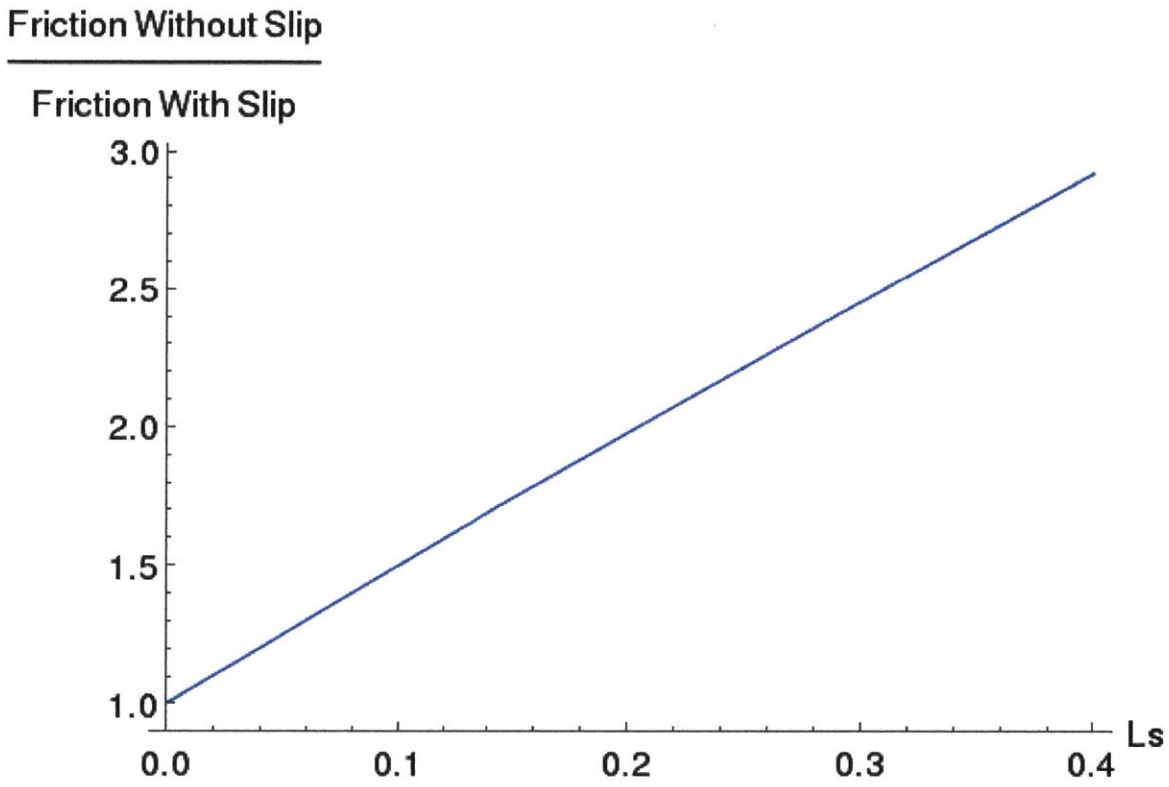

Figure 4-6: Ratio of the frictional force calculated from the slip corrected Reynolds equation to the frictional force calculated from the classical Reynolds equation with no-slip boundary conditions, at $x_2 = 1$, from Equation 4.11. All values have been non-dimensionalized as discussed in section 4.3. The plot shows that the overestimation of the frictional force is significant (~ 1.5 times) even when the minimum film thickness is 10 times the slip length.

as a function of x for the particular case $L_s/h_0 = 0.1$ and various values of the curvature parameter a; as expected, the general form of the pressure curve, (smoothly decreasing as we transition through the converging region into the diverging region of flow), is not altered by the inclusion of slip.

In general, the effect of slip can be described as reducing the resistance to flow (which can be also thought of as increasing the "effective film thickness"). The resulting effects are clearly demonstrated by the results discussed below, obtained for $aL^2/h_0 = 2$. Figure 4-4 shows that the maximum pressure is reduced as the slip length increases; for $L_s/h_0 = 0.1$, the pressure is overestimated by a factor of 1.5 when assuming no-slip. Figure 4-5 shows the ratio of the non-dimensional force (per unit depth) obtained using no-slip boundary conditions to that obtained using the slip boundary conditions, as a function of the slip length, L_s/h_0; it shows that the no-slip Reynolds solution overestimates the lift by about 1.5 times when the slip length is $\sim 0.1h_0$. The tendency of slip to reduce resistance to flow is exhibited in the frictional force measurements. As shown in Figure 4-6, the overestimation in the frictional force per unit depth, under a no-slip assumption, is about 1.5 when compared to when using a slip length of $\sim 0.1h_0$.

4.5 Molecular Dynamics simulation of the ring-liner gap

In this section we describe the results of our MD simulation of the ring-liner model. In the MD simulation, we use n-hexadecane as the lubricant, while the liner walls are modelled as BCC Fe (see Figure 2-2 for the geometry). Based on a characteristic lengthscale $L = 400$Å, the non-dimensional value of curvature parameter is $aL^2/h_0 = 1.845$. Our goal is to compare the pressure distribution obtained from the MD simulation with a computed analytical solution.

The MD simulation is performed at the same temperature (450 K) and a nominal pressure of 80 MPa as those used to derive the MODEL. This is necessary, since the

two descriptions will be compared as a means of validating the MODEL. We note that we are implicitly assuming that variations of the MODEL parameters (μ, L_s) with pressure are small (or conversely, pressure variations are sufficiently small that the variations in these parameters can be neglected); in the more general case, the parameters μ and L_s would need to be determined as a function of pressure and the MODEL solved by taking those variations into account. For a detailed discussion on the geometry used, the shear procedure, the method used to measure the pressure distribution from MD, including LAMMPS-specific details, refer to section 2.6.

4.5.1 Analytical solution

Let us now determine the pressure distribution analytically, by solving the MODEL using boundary conditions appropriate to the MD simulation described above. In general, the MODEL would have to be solved numerically, using, for example, a finite volume scheme. However, the MODEL obtained for the particular case considered in this thesis is the classical Reynolds equation corrected for slip; as we have seen earlier in this chapter, the solutions for a slip-corrected Reynolds equation, in the case of the barrel drop problem, are easy to compute analytically.

Starting from Eqn:4.2 we have

$$\frac{dp}{dx} = -\mu \frac{Q + Uh/2}{\frac{h^3}{12} + \frac{L_s h^2}{2}}$$

The boundary conditions for the pressure can be obtained by expressing the MD simulation conditions mathematically, as follows:

- $p(-L_x/2) = p(L_x/2) = p_0$, since periodic boundary conditions are imposed in the $\hat{\mathbf{x}}$ direction.
- $N = \int_{-L_x/2}^{L_x/2} p \, dx \times L_z$, where N is the total load applied on the MD system. As seen from Equation 4.12, the dominant force term in the $\hat{\mathbf{y}}$ direction comes from the pressure.

We also note that the pressure gradient also satisfies a periodic boundary condition, since $h(-L_x/2) = h(L_x/2)$.

Solving for the pressure, we obtain

$$p(x) = p_0 + \int_{-L_x/2}^{x} \mu \frac{-Q - Uh(x')/2}{\frac{h(x')^3}{12} + \frac{L_s h(x')^2}{2}}\, dx' \tag{4.13}$$

Applying the boundary conditions we obtain

$$Q = -\frac{\int_{-L_x/2}^{L_x/2} \frac{Uh(x')/2}{\frac{h(x')^3}{12} + \frac{L_s h(x')^2}{2}} dx'}{\int_{-L_x/2}^{L_x/2} \frac{1}{\frac{h(x')^3}{12} + \frac{L_s h(x')^2}{2}} dx'}$$

and p_0 is such that

$$N = p_0 L_x L_z + \int_{-L_x/2}^{L_x/2} \underbrace{\int_{-L_x/2}^{x} \mu \frac{-Q - Uh(x')/2}{\frac{h(x')^3}{12} + \frac{L_s h(x')^2}{2}} dx'}_{p_1(x)}\, dx \times L_z$$

It can easily be seen that the second term in the above equation is 0, since $p_1(x)$ is an odd function which is integrated over the interval $x \in [-L_x/2, L_x/2]$.

All the integrals involved in evaluating the constant Q were performed numerically using the Clenshaw-Curtis rule, using `Julia` package `Cubature` [52], with a maximum relative error of $\mathcal{O}(10^{-8})$.

4.5.2 Comparison of Molecular Dynamics results with MODEL results

Figure 4-7 shows the maximum variation in the pressure estimated by the analytical solution of the MODEL, as a function of the slip length. As seen before in Equation 4.6, increasing slip reduces the values of extremum pressures. Note that having a fluid of greater viscosity counters this effect and makes the peaks observed in the

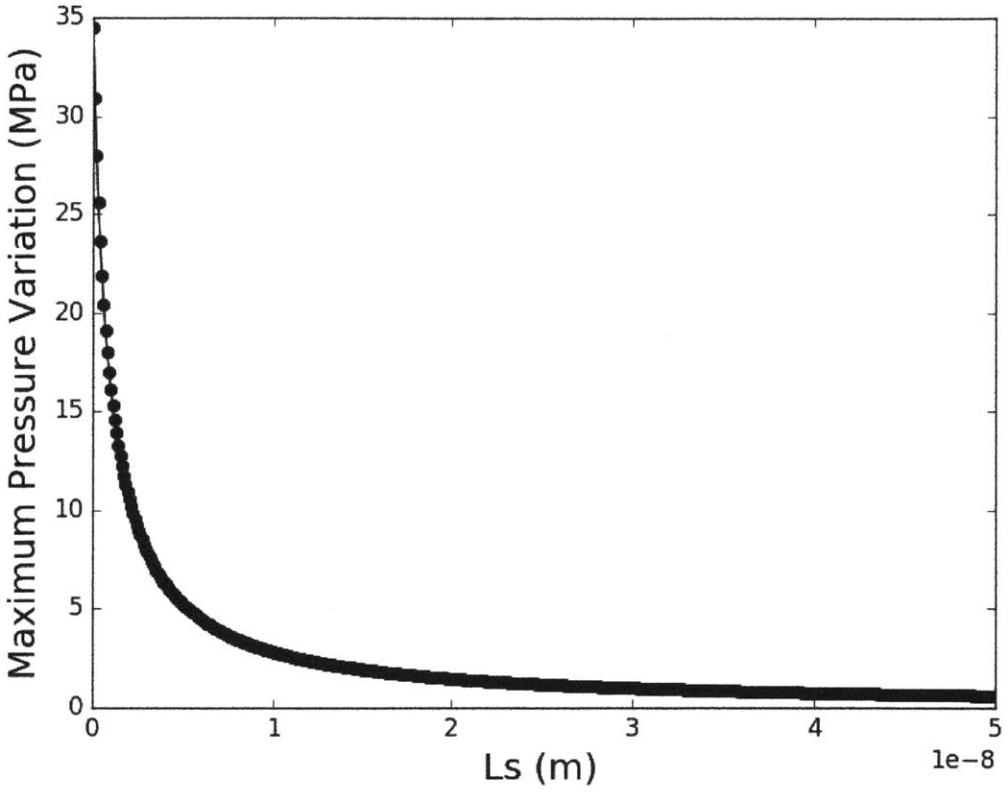

Figure 4-7: The maximum variation in the pressure distribution for values of slip lengths up to 50 nm, for a total load of $N = 1.2 \times 10^{-7}$ Newtons and $U = 60$ m/s.

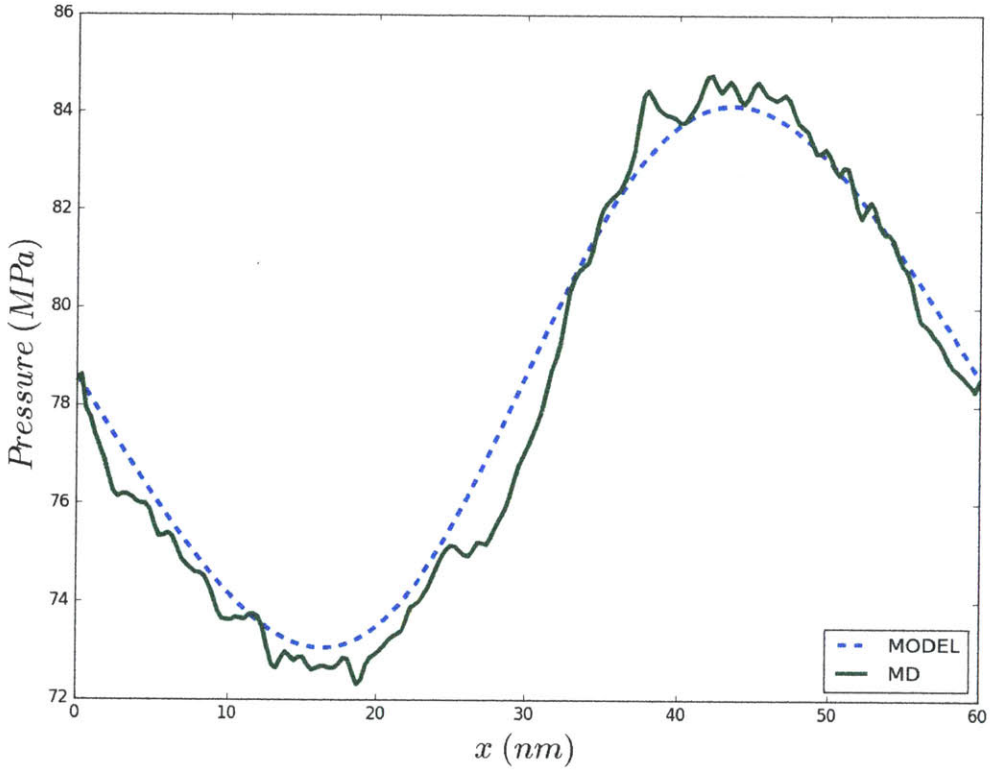

Figure 4-8: Comparison of MD pressure data against analytical solution for pressure computed using the MODEL.

pressure sharper. Figure 4-8 shows both the pressure distribution along $\hat{\mathbf{x}}$ computed from the analytical solution of the MODEL and that obtained from MD simulations. The MODEL derived in chapter 3, with a value of slip length $L_s = 2.1\ nm$ and a value of the coefficient of viscosity $\mu = 0.54\ mPa\ s$, produces results in excellent agreement with the estimated pressure from MD.

4.6 Conclusions

In this chapter we analyze the effect of slip on a simplified model of lubricant flow between the ring and the liner. Our results show that both the normal and frictional force on the ring surface are over-estimated by the no-slip boundary condition. For example, when $L_s/h_0 = 0.1$, both the normal and frictional forces are overestimated by a factor of 1.5 when compared to their corresponding no-slip solutions.

In the second half of the chapter we establish the validity of the MODEL in films of thicknesses as small as $\sim 4\ nm$ using the same ring-liner geometry but under different boundary conditions. Our MD simulations show that the dynamic pressure in the lubricant film closely follows the corresponding analytical pressure distribution computed from the MODEL. The good agreement between the lubrication equation solution and MD simulation leads us to conclude that generalizing Reynolds' equation to arbitrarily small gaps is both powerful and reliable, since it allows accurate calculation of pressure distributions in problems where the only other recourse would be molecular simulation.

We finally recall that in its present form, the MODEL consisted of a slip-corrected Navier-Stokes description, since it was found in chapter 3 to be a reliable description of the flow rate for all values of the gap height h considered in this work (i.e. both in the slip flow regime $h \gtrsim 5\ nm$, from where it originates, but also for $1\ nm < h < 5\ nm$). The case where the slip-corrected Navier-Stokes expression for the flow rate is not sufficiently accurate for small gap heights does not fundamentally alter the generality of the proposed approach; in such cases, a more general expression (fit) for the flow rate would need to be used—for example relation Equation 3.15 or even the more

general Equation 3.14 —with no other changes required.

Chapter 5

Effects of Slip on the TLOCR Model

In chapter 3 and chapter 4 we have shown that the applicability of the Navier-Stokes description and associated applications to lubrication can be extended to small characteristic lengthscales using insight from MD simulations and well-known theoretical constructs such as slip-flow theory. In this chapter we discuss how these ideas can be translated to IC engines where

- the complexity in the geometry of real engineering surfaces due to their surface-finish-dependent roughness, and
- the variable composition of both the solid surfaces and the lubricants complicated by lubricant additives, binding agents, friction modifiers etc,

make MD simulations that include all these effects difficult to perform.

In the interest of simplicity, in the present chapter we limit the discussion to the slip-corrected NS description (see Equation 3.13). In other words, we discuss how slip affects the hydrodynamic pressure in the lubricant between the Twin Land Oil Control Ring (TLOCR) and how existing calculation methods and models need to be modified in order to account for this effect. We also discuss how to obtain reliable values of the slip length from experimental measurements of the pressure and friction, since, as discussed above, realistic MD simulations of the engine environment are currently not possible.

The chapter is organized as follows. In section 5.1, we describe Chen's [20] model for obtaining the mean hydrodynamic pressure in the lubricant between the Twin Land Oil Control Ring(TLOCR) and the cylinder liner. This method relies on numerical results from Li's [65] deterministic method which is briefly described in section 5.1; modifications to Li's determinsitic method and Chen's TLOCR model are proposed in section 5.2 and section 5.3.

5.1 Overview of Chen's [20, 21] TLOCR model

In this section we provide an overview of Chen's method for approximately determining the average pressure and the shear stress in the lubricant between the TLOCR and the liner. This model, known as the *TLOCR model*, explicitly takes into account

- the nominal fluid film thickness,
- the roughness parameters of the liner micro-geometry,
- the sliding speed of the piston, and
- the dynamic viscosity of the lubricant

by utilizing sub-models for the hydrodynamic lubrication and the solid-solid contact.

This method has seen further improvements that consider the multiphase flow of the lubricant especially in the top two rings [20, 67]. The key purpose of Chen's model is to reduce the considerable complexity and computational cost of the complete method for estimating the lubricant pressure and shear stress, by running the full numerical solution for an extensive set of parameters (using the deterministic method discussed in the next section) and compiling its results into correlations.

These correlations have proved very useful in understanding various ring-liner shape and geometric effects on the ring tension, oil consumption and maximum hydrodynamic pressure and friction, which have subsequently led to design improvements such as minimization of the land width in the TLOCR [20], which is a widely used oil control ring in diesel engines. The correlation methodology is explained in

detail in [20, 67, 21]; here we discuss some aspects of the method in brief, in order to provide some context to the ensuing developments in this chapter.

The objective of the correlation method is the approximate prediction of the average hydrodynamic pressure, p_{hyd} (the hydrodynamic pressure averaged over the extent of the ring-liner overlap), average hydrodynamic friction, f_{hyd} and the oil consumption (flow rate), Q_{hyd}, during the engine cycle, at any given viscosity field, μ and the sliding speed, U. This is accomplished by the procedure outlined below (see [67, 20] for a detailed description).

Detemining the correlations

In developing the correlations, the following scaling assumptions are made:

$$p_{hyd}(\lambda, \mu, U) = \frac{\mu U}{\mu_0 U_0} p_h^{\mu_0, U_0}(\lambda) \tag{5.1}$$

$$f_{hyd}(\lambda, \mu, U) = \frac{\mu U}{\mu_0 U_0} f_h^{\mu_0, U_0}(\lambda) \tag{5.2}$$

$$Q_{hyd} = \frac{U}{U_0} Q_h^{U_0}(\lambda) \tag{5.3}$$

In the above, $p_h^{\mu_0,U_0}$, $f_h^{\mu_0,U_0}$ and $Q_h^{U_0}$ are the hydrodynamic pressure, hydrodynamic shear force and the oil flow rate, respectively at the reference μ_0 and sliding speed U_0; these functions are determined by running the deterministic solver at the reference viscosity and sliding speed at various different film thickness ratios λ given by,

$$\lambda = D/\sigma_p, \tag{5.4}$$

where, D, is the distance between the mean level of the plateau roughness of the liner and the ring surface and σ_p is the RMS roughness of the plateau region of the liner. These scaling relations have been validated in section 3.6 of Haijie Chen's Master's thesis [20]. The deterministic method, whose details we consider in the next section, is a numerical method for the solution of the unsteady Reynolds equation that considers the mesoscale roughness of the liner in its plateau region.

Load balance is satisfied by combining the hydrodynamic pressure, determined

from the above correlations, with the average contact pressure, p_{con}, namely,

$$p_{ocs} = p_{hyd}(\lambda, \mu, U) + p_{con}(\lambda) \tag{5.5}$$

where, p_{ocs} is the normal load applied by the oil control ring (See Figure 1-1). The average contact pressure is determined from a simplified version [47] of the Greenwood-Tripp [38] asperity contact model

$$p_{con} = \begin{cases} p_k \times (\Omega - h/\sigma_p)^z & h/\sigma_p < 4.0 \\ 0 & h/\sigma_p > 4.0 \end{cases} \tag{5.6}$$

where the parameter p_k depends on the elastic properties of the ring and liner surfaces, such as the Young's modulus and the Poisson ratio. For a typical configuration of a cast iron liner and a steel ring, this parameter is taken to be equal to 2.0486×10^4 Pa [21, 67]; Ω in the above equation is taken as 4 for the non-Gaussian surface used in this thesis [21], while z = 6.804 [47]. The average pressure from the asperity contact model was found to be approximately 23 *bar* for the surface used, at the film thickness ratio of 2 studied in this thesis.

Given the above hydrodynamic and the contact sub-models, the computation proceeds as follows: For a given pressure from the oil control ring, the film thickness ratio, λ, during the cycle, is solved for from Equation 5.5. The resulting value of λ is used to calculate the frictional force, through the correlation for the frictional force obtained in the hydrodynamic sub-model. This frictional force is integrated over the engine cycle, to obtain the Friction Mean Effective Pressure (FMEP). In the following section, we outline the methodology behind Li's [65] solver for obtaining the correlations that form the hydrodynamic sub-model.

5.1.1 Introduction to Li's [65] deterministic solver

Li's [65] method for solving for the lubricant pressure includes consideration of the composite micro-roughness of the liner surface. This method, which uses a Finite

Volume scheme to solve a Reynolds equation that accounts for cavitation in regions of low pressure, is part of a suite of tools associated with Tian's cycle model [105], developed for describing the lubrication dynamics of the piston ring pack-liner system.

Since obtaining surface measurements experimentally at the resolution level required in the numerical solution is difficult, the deterministic method uses numerically generated surfaces that have the same statistical roughness parameters as real liner surfaces [20, 12]. Each generated surface is sampled at many representative *phases* (as discussed in subsection 1.1.2) in the plateau region that capture surface measurements at different patches on the plateau part of the liner.

The determinisitic method solves the unsteady Reynolds equation at a given thickness ratio, for a given surface, for all the *phases*; the average hydrodynamic pressure and the average hydrodynamic friction are then calculated by taking the average over all phases, of the spatial average over the domain, of the computed hydrodynamic pressure and friction distributions, respectively.

5.1.2 Deterministic solution of the Reynolds equation

The classical Reynolds equation for a compressible liquid, in two dimensions, is given by:

$$\frac{\partial(\rho h)}{\partial t} = \frac{\partial}{\partial x}\left(\frac{\rho h^3}{12\mu}\frac{\partial p}{\partial x}\right) + \frac{\partial}{\partial z}\left(\frac{\rho h^3}{12\mu}\frac{\partial p}{\partial z}\right) - \frac{U}{2}\frac{\partial(\rho h)}{\partial x} \tag{5.7}$$

where, $U\,\hat{\mathbf{x}}$ is the constant velocity of the ring with respect to the liner and ρ is the density of the lubricant. When the pressure in the lubricant falls below the cavitation pressure at any point, the lubricant exists as vapor-liquid mixture or a *partial film* at a constant pressure. The pressure gradient terms in the Reynolds equation therefore have no effect in these pockets of low pressure and the governing equation becomes a hyperbolic conservation law, given by [20]

$$\frac{\partial(\rho h)}{\partial t} = -\frac{U}{2}\frac{\partial(\rho h)}{\partial x}. \tag{5.8}$$

To avoid local numerical instabilities [85] that arise due to switching from the convection-diffusion equation in Equation 5.7 to the hyperbolic Equation 5.8 when the pressure falls below the cavitation pressure, and simultaneously ensure fast convergence, the Reynolds equation is solved for the *universal variable*, α, defined as follows [20, 67, 21]:

$$\alpha = \frac{p - p_c}{p_{ref}} + 1, \qquad \text{in the full film zone} \tag{5.9}$$

$$\alpha = \rho/\rho_c = \phi, \qquad \text{in the cavitation zone} \tag{5.10}$$

where p_{ref} is the ambient pressure usually taken to be the atmospheric pressure and ρ_c is the vapor density in the cavitation zone. That is, the universal variable represents a dimensionless pressure in the full film zone and the volume ratio, $\phi = \rho/\rho_c$ in the cavitation zone (see Section 3.2 of Yong Li's PhD thesis [65] for the rationale behind choosing the universal variable to be two different physical quantities in the cavitation and the full region). Dividing the Reynolds equation in Equation 5.7, by ρ_c, we obtain the following non-linear equation for α,

$$F(\alpha, h) =$$
$$-\frac{\partial(\phi(\alpha)h)}{\partial t} + \frac{\partial}{\partial x}\left(\frac{\phi(\alpha)h^3}{12\mu}\frac{\partial p(\alpha)}{\partial x}\right) + \frac{\partial}{\partial z}\left(\frac{\phi(\alpha)h^3}{12\mu}\frac{\partial p(\alpha)}{\partial z}\right) - \frac{U}{2}\frac{\partial(\phi(\alpha)h)}{\partial x} = 0 \tag{5.11}$$

Li [65] applies a classical implicit Finite Volume scheme on the above equation, to obtain the discrete system, $\tilde{F}(\tilde{\alpha}, \tilde{h}) = 0$, and solves for $\tilde{\alpha}$. By the convenient definition of the universal variable in Equation 5.10 and choosing p_{ref} to be p_c, we can observe that a Finite Volume node is in the full film zone if $\tilde{\alpha} > 1$, at the node. A binary index variable is used to indicate if a node is in the full film or the partial film region and the appropriate governing equation is solved at the node, based on the value of the index variable. That is, the Poiseuille flow rate terms (the 2nd and 3rd terms on the right hand side of Equation 5.11) are set to 0 whenever the value of the index variable indicates cavitation, thus reducing the governing equation to Equation 5.8 in the cavitation zone. To ensure continuity in the mass flow rate, Li [65] designs an

iterative scheme that uses Newton's method to solve the non-linear Equation 5.11. The Jacobian used in the Newton iterations can be written as

$$\frac{\partial \tilde{F}}{\partial \tilde{\alpha}} = \frac{\partial \tilde{F}}{\partial \tilde{\phi}} \frac{\partial \tilde{\phi}}{\partial \tilde{\alpha}} + \frac{\partial \tilde{F}}{\partial \tilde{p}} \frac{\partial \tilde{p}}{\partial \tilde{\alpha}}, \tag{5.12}$$

using $\tilde{}$ to represent discretized quantities in the Finite Volume solution of Equation 5.11. The partial derivatives $\frac{\partial \tilde{F}}{\partial \tilde{\phi}}$ and $\frac{\partial \tilde{F}}{\partial \tilde{p}}$ become clear on establishing a discretization scheme.

Li's [65] iteration scheme ensures the convergence of the status of each node (whether it is in the full film or the partial film region) to a steady value after which the equation for the universal variable in Equation 5.11 (a linear equation in either case of full or partial film) is solved to get the hydrodynamic pressure distribution. For a detailed description of the deterministic solver see chapter 3 of Yong Li's PhD thesis [65]. In the next section, we describe the modifications required include slip effects.

5.2 Numerical solution of Reynolds equation with slip: modifications to the deterministic method

In this section we study the steady solution of the modified Reynolds Equation, for a particular liner surface (provided by Daimler) with a non-Gaussian distribution, with $Ra = 21nm$ and $\sigma_p = 51nm$, at a particular phase, and discuss the effects of slip on the computed average hydrodynamic pressure and the shear stress.

The first observation to be made in revising the formulation of the governing equation in the deterministic method is that slip effects are not felt in the partial film region, since the Couette part of the flow rate is unaffected by slip (see chapter 3 for more details). Including the first order slip correction into the above formulation,

modifies the governing equation in Equation 5.7 for the *full film*, as follows:

$$\frac{\partial(\rho h)}{\partial t} = \frac{\partial}{\partial x}\left(\left(\frac{\rho h^3}{12\mu} + \frac{\rho L_s h^2}{2\mu}\right)\frac{\partial p}{\partial x}\right) + \frac{\partial}{\partial z}\left(\left(\frac{\rho h^3}{12\mu} + \frac{\rho L_s h^2}{2\mu}\right)\frac{\partial p}{\partial z}\right) - \frac{U}{2}\frac{\partial(\rho h)}{\partial x} \quad (5.13)$$

In the above equation, L_s is the slip length, that could exhibit spatial variation, depending on the local liner roughness. In the interest of simplicity, we assume a constant slip length in this thesis; we also propose a modified determinsitic correlation method to obtain the average value of this slip length.

The non-linear equation for the universal variable that is iteratively solved via a Newton's method is now given by

$$\begin{aligned} F(\alpha, h) = &-\frac{\partial(\phi(\alpha)h)}{\partial t} + \frac{\partial}{\partial x}\left(\left(\frac{\phi(\alpha)h^3}{12\mu} + \frac{\phi(\alpha)L_s h^2}{2\mu}\right)\frac{\partial p(\alpha)}{\partial x}\right) \\ &+ \frac{\partial}{\partial z}\left(\left(\frac{\phi(\alpha)h^3}{12\mu} + \frac{\phi(\alpha)L_s h^2}{2\mu}\right)\frac{\partial p(\alpha)}{\partial z}\right) - \frac{U}{2}\frac{\partial(\phi(\alpha)h)}{\partial x} \end{aligned} \quad (5.14)$$

Following Li's method, we solve the steady state form of the above equation at phase 0. We set $\lambda = 2$, which is the minimum clearance solved for in Chen's[20] TLOCR model. The influence of slip phenomena becomes larger as the mediating gap decreases, since the slip length is usually in the order of a few nanometers.

The initial guess for the pressure used in Newton's method is a constant distribution of 2 bar at all points. For a tolerance of $1.e-8$ in relative error, we achieve convergence within a maximum of 80 iterations, at any phase of the liner roughness. In the following subsections, we discuss modifications required to the deterministic solver to include slip effects.

5.2.1 The threshold for contact

As Chen notes (see Figure 2.4 of [20]), in regions where the clearance between the ring and the liner are small, "unrealistically" high pressures were obtained in the deterministic method. As a work around, a *cut-off* is used for clearances below which the hydrodynamic pressure is not estimated, thereby implicitly assuming asperity

contact at those points. This cut-off clearance was chosen to be 10 nm in Chen and Liu's work.

In the present work, this cut-off is taken to be 4 nm, motivated by the threshold we observed in chapter 3 for Navier-Stokes validity. The rationale behind lowering the cut-off is that the previous cut-off of 10 nm is pessimistic. This is because, even molecularly thin lubricant films are known to withstand very high pressures and protect the surfaces from contact and wear. Zheng et al. [115] give an estimate of $\sim 1\ GPa$ for the film rupture of n-alkanes with a chain length of 32; real lubricants are generally longer, branched alkanes with higher load carrying capacity. In comparison, the maximum local pressures observed in the deterministic method, even in regions of very thin (e.g. 4 nm) films tends to be less than 1 GPa, when slip is included.

Although lowering the cut-off is reasonable, a MODEL for these complex systems currently does not exist. On the other hand, the present modified deterministic approach is strictly only valid when the minimum film thickness is such that the Navier-Stokes description is still valid and the pressure is lower than the threshold for film squeeze-out. Unfortunately, both of these validity limits are difficult to estimate in the dynamic engine environment. As a result, we use a cut-off of 4 nm in this chapter with the understanding that only at points of zero or negative clearances does asperity contact actually occur. In the present deterministic method, the pressure due to asperity contact is only added as an averaged effect, for a given mean clearance between the surfaces. A deterministic method which includes grid-resolved asperity contact pressures would be an enormous improvement over the current model.

5.2.2 Changes in the system setup

Besides the change in the function $F(\alpha, h)$, from Equation 5.11 to Equation 5.14, the Jacobian should also change to include the addition of the slip terms. Consider a Finite Volume node, i, centered at (x_i, z_i), that has an extent of Δx in $\hat{\mathbf{x}}$ and Δz in $\hat{\mathbf{z}}$, in the full film region. If the spatial derivatives were discretized using a backward difference, the term, $\dfrac{\partial \tilde{F}}{\partial \tilde{p}}$, that goes into Equation 5.12, is given by:

$$\left.\frac{\partial \tilde{F}}{\partial \tilde{p}}\right|_{i,t+\Delta t} = -\frac{1}{\Delta x}\left(\frac{\tilde{h}^3}{12\mu}+\frac{L_s\tilde{h}^2}{2\mu}\right)\Big|_{x_i+\Delta x/2,z_i} - \frac{1}{\Delta x}\left(\frac{\tilde{h}^3}{12\mu}+\frac{L_s\tilde{h}^2}{2\mu}\right)\Big|_{x_i-\Delta x/2,z_i}$$
$$- \frac{1}{\Delta z}\left(\frac{\tilde{h}^3}{12\mu}+\frac{L_s\tilde{h}^2}{2\mu}\right)\Big|_{x_i,z_i+\Delta z/2} - \frac{1}{\Delta z}\left(\frac{\tilde{h}^3}{12\mu}+\frac{L_s\tilde{h}^2}{2\mu}\right)\Big|_{x_i,z_i-\Delta z/2} \quad (5.15)$$

Due to the implicit (in time) method used, in the above equation, $\tilde{h}$ denotes the gap height evaluated at the solution timestep, namely $\tilde{h}(t+\Delta t)$. The value of $\tilde{h}$ was taken to be the mean of the nodal values on the two sides of the respective nodal interfaces indicated in the above equation.

5.2.3 Mass flow rate

The inclusion of slip effects into the deterministic solver is complete with the addition of the slip terms in the non-linear equation and modifying the Jacobian as described above. We verified that the continuity in the mass flow rate is maintained automatically. This is not a surprise since the iteration scheme, by design, ensures that the mass flow rate is conserved. Including slip effects increases this flow rate but the new flow rate is the same across all nodes.

5.3 Results and Discussion

Figure 5-1 shows a measure of the film thickness distribution at phase 0. Due to the large variation in these values, in the figure we plot the negative logarithm of the film thickness measured in meters. The calculated pressure distribution without slip (at phase 0) is shown in the bottom half of Figure 5-2; the corresponding calculated pressure including a slip correction ($L_s = 5\ nm$) results in the pressure distribution shown in the top half of Figure 5-2. The white regions in the figure are points where the clearance is less than 4 nm, whereby the hydrodynamic pressure was not calculated. At the outset, we observe that the pressures estimated when considering a no-slip boundary condition are much higher than those computed in the presence

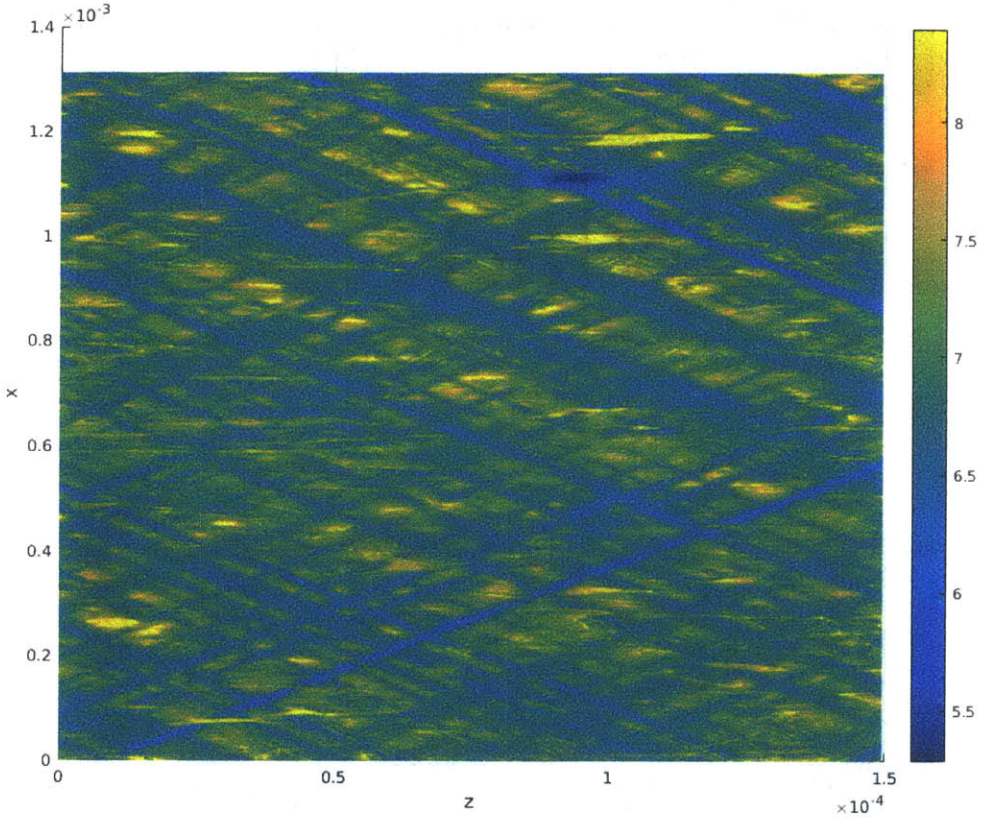

Figure 5-1: The negative logarithm of the film thickness distribution in meters at evenly spaced grid points at phase 0. Thicknesses below the cut-off, 4 nm, were set to 4 nm in this figure. The maximum film thickness in the above figure was 5 μm and the mean film thickness was 169.88 nm.

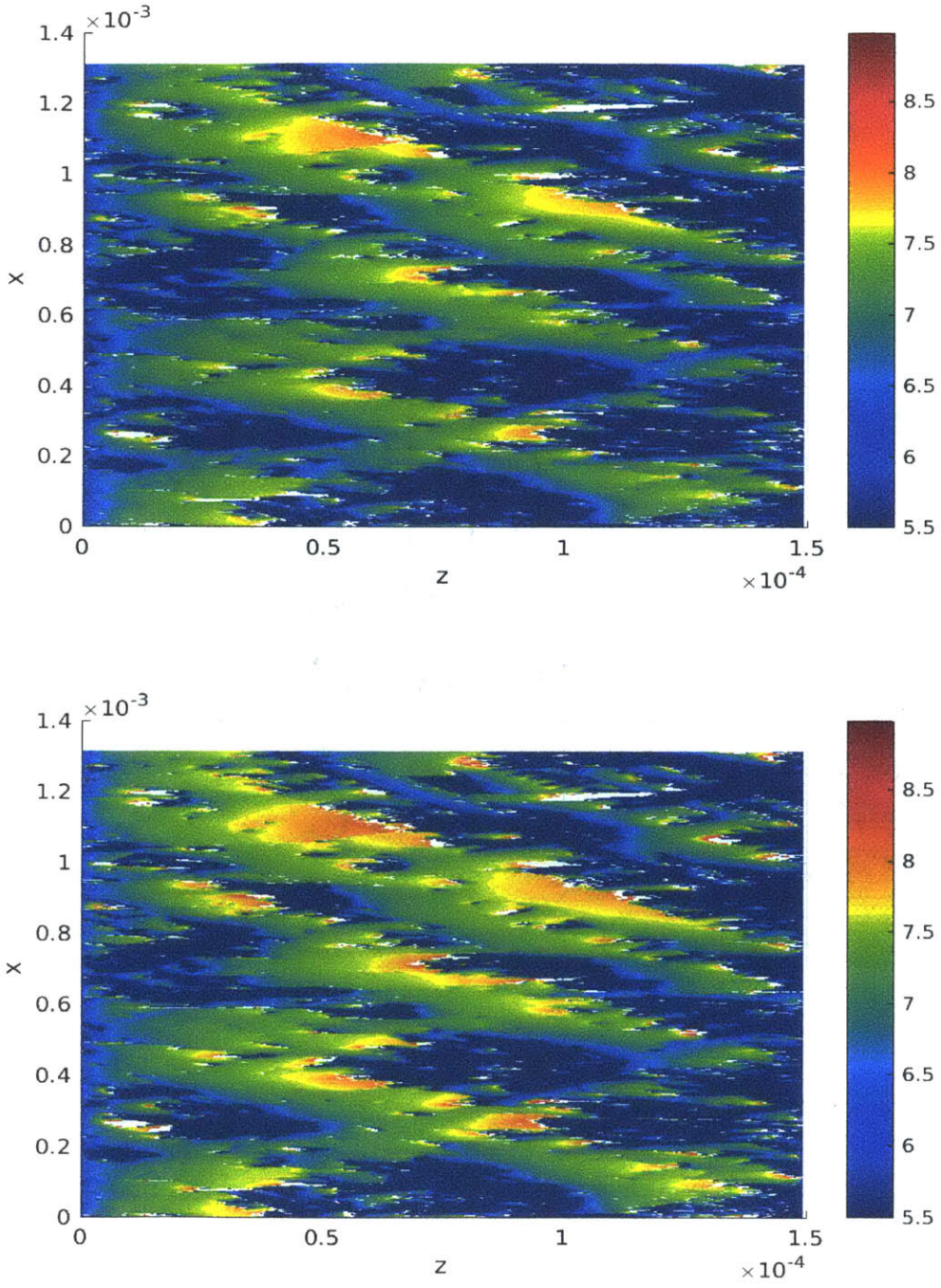

Figure 5-2: The logarithm of the hydrodynamic pressure in Pa at evenly spaced grid points. The top figure shows the pressures computed accounting for slip, at a slip length of 5 nm and bottom figure, using Chen and Liu's original TLOCR program.

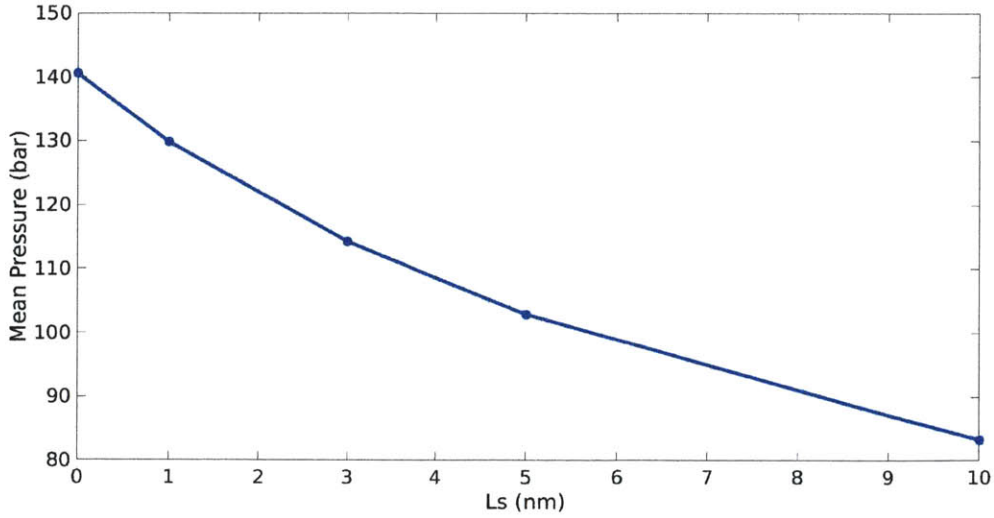

Figure 5-3: The mean pressure at phase 0 as a function of the slip length.

of the slip correction terms. The mean pressure at phase 0 was found to be 103 bar with a slip of 5 nm. The mean pressure calculated in the absence of slip was 140 bar or 35% higher in comparison. Neglecting slip results in an overestimation of the *maximum* hydrodynamic pressure by 3.4 times, when compared to when using a slip length of 5 nm.

Figure 5-3 shows that the mean pressure observed decreases considerably as the slip length increases. The shear force per unit area at the mean liner roughness is given by

$$\mu \frac{\partial u}{\partial y}\bigg|_{y=0} = \frac{U\mu}{h + 2L_s} - \frac{dp}{dx}\frac{h}{2}.$$

The shear force computed at the nodes at smaller film thicknesses ($\sim \mathcal{O}(L_s)$) are expected to show, therefore, a significant reduction; the overall reduction, when summed over the domain, is not as large as that in the pressure ($\sim$ 15% at a slip length of 10 nm), as shown in Figure 5-4. The increase in the overall flow rate is much smaller, namely $\sim$ 2% for slip lengths up to 10 nm.

Based on these numerical results obtained from the modified steady state solver at phase 0, we suggest the following further modifications to the deterministic solver and to the correlation method discussed in the beginning of this chapter.

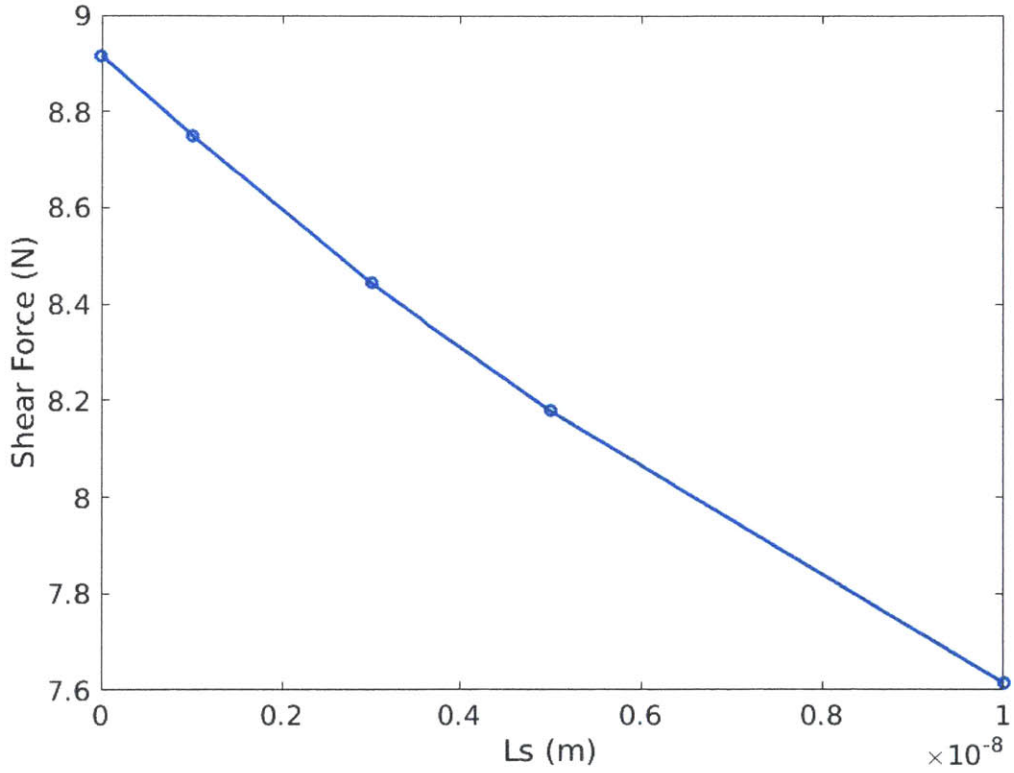

Figure 5-4: The variation in the mean shear force exerted by the lubricant at phase 0, as a function of the slip length.

5.3.1 The slip constitutive relationship

Deriving the slip constitutive relationship for a real piston ring-liner contact is a very challenging problem, as described in the introduction to this chapter. Given the composite roughness of the liner surface and the worn surface of the liner, the slip length may not be a constant throughout the domain. Including the slip length as a parameter in the correlation method can be done, as a first approximation, in an average sense. In order to find improved correlations that include this average slip length, we need reference results for varying film thickness ratios *and* slip lengths at the reference sliding speed and viscosity. Subsequently, the film thickness ratios and the average slip length can then be retrieved from the experimental data from the following inverse problem:

$$\begin{bmatrix} \langle p_{hyd}(\lambda, L_s, \mu, U) + p_c(\lambda) \rangle \\ \langle f_{hyd}(\lambda, L_s, \mu, U) + f_c(\lambda) \rangle \end{bmatrix} = \begin{bmatrix} p_{ocs} \\ FMEP \end{bmatrix} \tag{5.16}$$

where $p_{hyd}(\lambda, L_s, \mu, U)$ and $f_{hyd}(\lambda, L_s, \mu, U)$ are the average hydrodynamic pressure and the average friction per unit area, at a point during the cycle, with sliding speed U and viscosity field, μ, to be obtained from the new correlations; $\langle \cdot \rangle$ represents the average over the piston cycle. $FMEP$ denotes the Friction Mean Effective Pressure and p_{ocs} represents the mean pressure exerted by the oil control spring during the cycle.

The disadvantage of the above approach for estimating the value of the slip length is that the values of the oil control spring pressure are difficult to isolate in experiments [20].

5.4 Summary

We have incorporated a slip correction into the deterministic solver for the Twin Land Oil Control Ring-Liner lubrication model. We obtain the numerical solutions for the pressure, shear force and the flow rate in a part of the gap between the ring land width

and the plateau part of the liner roughness. Our findings have important implications for improving both the accuracy and fidelity of the deterministic correlation method [20, 67, 65] in the following ways:

- With no significant additional computational effort, slip effects can now be included into the deterministic solver. The correlation method can now access nominal clearances lower than the previous limit of $2\sigma_p$ without obtaining unphysical, high pressures.

- At a nominal separation of $2\sigma_p$, we observe that including the effect of slip causes a significant decline in the mean pressure that increases with increase in the slip length.

- The effect of slip is also to decrease the hydrodynamic shear force exerted by the lubricating oil by a 15% margin at a slip length of 10 nm.

- While a MODEL-type approach may be difficult to obtain for a realistic ring-liner contact, the overall effect of slip on the TLOCR model could be seen by parameterizing the scaling relations for different values of (domain-averaged) slip length.

Chapter 6

Summary and Future Work

We have presented a continuum lubrication equation for modeling problems involving scales sufficiently small that the Navier-Stokes description breaks down. This was achieved by combining a more general flow rate constitutive relation with the mass conservation equation (given here in one dimension),

$$\frac{\partial h}{\partial t} + \frac{\partial Q}{\partial x} = 0 \tag{6.1}$$

to obtain a Reynolds-type equation, referred to as MODEL or Molecular Dynamics-based Equation for Lubrication. In the present work we focussed on a simplified lubricant, n-hexadecane, bounded by smooth Fe walls at a temperature of 450 K and a pressure of approximately 80 MPa. The methodology however, is completely general and can be applied to any liquid state of interest.

The more general flow rate constitutive relation was based on a slip-corrected Poiseuille flow rate. This choice ensures that the flow rate asymptotically captures both the slip-flow and the no-slip (large scale) regimes naturally and with no unphysical parameters. As a matter of reference, for the system studied here, slip appears to become non-negligible (contributes more than 5%) for gap heights smaller than 240 nm. We therefore define the slip-flow regime, *for the system studied here*, as the film thickness range 5 $nm \lesssim h \lesssim$ 240 nm. The lower bound of 5 nm has been determined by our MD simulations as the approximate lengthscale at which the

Navier-Stokes, and thus the slip-flow description, breaks down. At this lengthscale the flow rate predicted by slip-flow is approximately 3.5 times larger than the flow rate predicted by the no-slip description.

Remarkably, our MD simulations show that the slip-corrected Poiseuille flow rate, with a *fixed* slip length determined from MD data in the slip-flow regime, correctly predicts flow rates for film thicknesses as small as 1 nm without requiring a correction for films smaller than approximately 5 nm for which the Navier-Stokes description is not valid. This is rather surprising and we believe is a result specific to the system studied here. In other systems, we expect that the general constitutive relation will have to account for some deviations from slip-corrected flow rates.

We validate the MODEL using a barrel-drop model of the lubrication flow between one of the top two rings and the liner. The pressure distribution predicted by the MODEL shows excellent agreement with that observed in the MD simulation of the same problem.

Subsequently, we analyze the effect of slip in the Twin Land Oil Control Ring (TLOCR) - Liner lubricated system in an IC engine, where application of the MODEL is more challenging. We find that introducing a slip correction to the hydrodynamic model of the TLOCR produces a significant change in the pressure distribution. At a slip length of 5 nm, the maximum pressure is found to be $3-4$ times lower than that obtained in the absence of slip; the frictional force was observed to change by $10-15\%$, while the change in the overall oil consumption is negligible. Based on these results we propose that the correlations for the pressure and the friction obtained in the TLOCR model be augmented to include the slip correction.

6.1 Future work

Although continuum models, like the one derived in this thesis, are superior to particle methods in terms of computational cost, the latter have some distinctive advantages, namely, the ease of modeling arbitrarily complex geometries and fluid-structure interaction as well as their automatic inclusion of non-continuum effects as they naturally

arise. Boundary lubrication has presented elusive challenges precisely because it involves a complex coupling of hydrodynamics and solid mechanics, at lengthscales where continuum models for fluids and solids may be invalid. Hence, particle-based methods, although inefficient, may be better suited to boundary lubrication problems.

As discussed in the introduction, the lengthscales of roughness of surfaces and the film thickness of the mediating lubricant in a boundary lubricated region, could span a few nanometers to a few hundred nanometers. Since MD is practical only on the lower end of these length scales, hybrid methods that combine atomistic simulations with continuum approaches [111] can be used although they are hard to implement. Methods such as Smooth Particle Hydrodynamics [79] are not useful in boundary lubrication since they make the explicit assumption of the validity of Navier-Stokes theory.

Among the existing methods, Dissipative Particle Dynamics (DPD) [46, 30] has been used widely in modelling settings of shear flows of complex fluids [56, 33, 32]. In Español and Warren's [30] formulation of DPD, all particles interact through 3 forces: a conservative force, $\mathbf{F}_c$, a dissipative force, $\mathbf{F}_d$, and a random force, $\mathbf{F}_r$. The dissipative and random components together conserve momentum locally, serve as a thermostat and mimic the viscous and pressure forces of a fluid of a certain viscosity [30, 28]. The conservative force models the "soft" repulsion among fluid elements.

Unfortunately, standard DPD is also expected to be limited to Navier-Stokes behavior [46, 30]. In fact, it has been shown through various statistical mechanics approaches that the hydrodynamic equations for DPD are the Navier-Stokes equation [71, 28]. DPD is also unsuitable for boundary lubrication since the flow boundary conditions are currently input to the model (cannot be deduced from the simulations), unlike fullly atomistic descriptions such as MD. Usually, in polymer flows, the parameter for the wall-fluid repulsion chosen indirectly from Flory-Huggins theory gives the expected mesoscopic boundary conditions at the wall [39]. Relating the DPD timescales and lengthscales to physical models remains difficult since DPD fluids do not replicate real dynamic behavior under shear (for example, the ratio of the viscosity to the diffusion coefficient may be different from real fluids for DPD fluids)

[54, 39].

A recent powerful approach proposed by Hijòn et al. [45] can overcome some of these limitations. In their approach, Hijòn et al. [45] derive a general equation for a coarse-grained fluid [29] from the Generalized Langevin Equation (GLE), using Zwanzig's projection operator formulation [117]. The only approximation made in reducing the complex integro differential (Generalized Langevin) equation to a DPD-like equation (referred to as the Markovian asssumption), is that the irrelevant subspace of dynamical variables (whose motion is not explicitly tracked) evolves infinitely fast when compared to the relevant subspace consisting of the coarse-grained variables. In DPD-like equation for the evolution of the coarse-grained variables obtained by Hijòn et al., the conservative and friction forces depend on the dynamics of all the relevant variables and are hence computed through constrained Molecular Dynamics simulations.

This procedure holds some promise with regard to modelling boundary lubrication problems at the mesoscale. For complicated polymer molecules that constitute lubricants, where the degree of coarse-graining is to the level of center of mass of a group of polymer molecules, the Markovian assumption seems reasonable. Finding the nature of the forces between the elastic solid walls and the fluid particles involves evaluating high-dimensional conditional expectations over the full atomistic phase space. Models for these forces using the projection operator formalism, for both solids and fluids, exist [25, 92, 45] but only for systems with simple quadratic Hamiltonians. Identifying the correct fluid-fluid, wall-fluid and wall-wall interactions at a given level of coarse-graining remains an open problem, that if solved, could be input into the above described bottom-up models for coarse-grained system dynamics. These could pave the way for sophisticated coarse-grained particle simulations that would enhance our understanding of not just boundary lubrication but that of generalized mesocopic fluid-solid interactions.

Bibliography

[1] G. J. Ackland, D. J. Bacon, A. F. Calder, and T. Harry. Computer simulation of point defect properties in dilute Fe-Cu alloy using a many-body interatomic potential. *Philosophical Magazine A*, 75(3):713–732, 1997.

[2] F. J. Alexander, A. L. Garcia, and B. J. Alder. Direct Simulation Monte Carlo for thin-film bearings. *Physics of Fluids*, 6(12):3854–3860, 1994.

[3] M. P. Allen and D. J. Tildesley. *Computer simulation of liquids.* Oxford University Press, 1991.

[4] E. Bardasz, D. Mackney, N. Britton, G. Kleinschek, K. Olofsson, I. Murray, and A. P. Walker. Investigations of the interactions between lubricant-derived species and aftertreatment systems on a state-of-the-art heavy duty diesel engine. *SAE 2003 Transactions Journal of Fuels and Lubricants*, 112, 2003.

[5] J.-L. Barrat and L. Bocquet. Influence of wetting properties on hydrodynamic boundary conditions at a fluid/solid interface. *Faraday Discussions*, 112:119–128, 1999.

[6] J.-L. Barrat and L. Bocquet. Large slip effect at a nonwetting fluid-solid interface. *Faraday Discussions*, 82(23):4671, 1999.

[7] H. Berro, N. Fillot, and P. Vergne. Molecular dynamics simulation of surface energy and ZDDP effects on friction in nano-scale lubricated contacts. *Tribology International*, 43(10):1811–1822, 2010.

[8] B. Bhushan. *Principles and applications of Tribology.* John Wiley & Sons, Inc., 1999.

[9] B. Bhushan, J. N. Israelachvili, and U. Landman. Nanotribology: friction, wear and lubrication at the atomic scale. *Nature*, 374:607–616, 1995.

[10] I. Bitsanis, J. J. Magda, M. Tirrell, and H. T. Davis. Molecular dynamics of flow in micropores. *The Journal of Chemical Physics*, 1987.

[11] L. Bocquet and J.-L. Barrat. Flow boundary conditions from nano- to micro-scales. *Soft Matter*, 3, 2007.

[12] N. W. Bolander, F. Sadeghi, and G. R. Gerber. Piston ring friction reduction through surface modification. *ASME Internal Combustion Engine Divison 2005 Fall Technical Conference*, 2005.

[13] W. M. Brown, A. Kohlmeyer, S. J. Plimpton, and A. N. Tharrington. Implementing molecular dynamics on hybrid high performance computers - particle-particle particle-mesh. *Computer Physics Communications*, 183:449–459, 2012.

[14] W. M. Brown and Y. Masako. Implementing molecular dynamics on hybrid high performance computers- three-body potentials. *Computer Physics Communications*, 184:2785–2793, 2013.

[15] W. M. Brown, P. Wang, S. J. Plimpton, and A. N. Tharrington. Implementing molecular dynamics on hybrid high performance computers - short range forces. *Computer Physics Communications*, 182:898–911, 2011.

[16] A. Cameron. *Basic lubrication theory.* Ellis Horwood Ltd., 1983.

[17] V.A. Carrick, G.D. Lamb, E.A. Bardasz, and W.D. Abraham. Lubricating oil composition, June 24 2003. US Patent 6,583,092.

[18] J. Casado-Díaz, E. Fernàndez-Cara, and J. Simon. Why viscous fluids adhere to rugose walls: A mathematical explanation. *Journal of Differential Equations*, 189(2):526–537, 2003.

[19] N. Chandramoorthy. Thesis scripts. `https://github.com/nishaChandramoorthy/SMThesis`. Input and post-processing scripts used in this work.

[20] H. Chen. Modelling of liner finish effects on oil control ring lubrication in internal combustion engines based on deterministic method. Master's thesis, Massachusetts Institute of Technology, 2008.

[21] H. Chen. *Modeling the lubrication of the piston ring pack in Internal Combustion engines using the deterministic method.* PhD thesis, Massachusetts Institute of Technology, 2011.

[22] H. Chen and T. Tian. The influences of cyliner liner honing patterns and oil control ring design parameters on the interaction between the twinland oil control ring and the cylinder liner in internal combustion engines. *2008 SAE International Powertrains, Fuels and Lubricant Congress*, 2008.

[23] S. Chen and G. D. Doolen. Lattice Boltzmann method for fluid flows. *Annual Review of Fluid Mechanics*, 30(1):329–364, 1998.

[24] C. Cottin-Bizonne, A. Steinberger, B. Cross, O. Raccurt, and E. Charlaix. Nanohydrodynamics: The intrinsic flow boundary condition on smooth surfaces. *Langmuir*, 24, 2008.

[25] D. Cubero and S. Yaliraki. Inhomogeneous multiscale dynamics in harmonic lattices. *Journal of Chemical Physics*, 122(3), 2005.

[26] D. Dowson. A generalized Reynolds equation for fluid-film lubrication. *Langmuir*, 12, 1996.

[27] D. Dowson and G. R. Higginson. *Elastohydrodynamic lubrication.* Pergamon Press, 1966.

[28] P. Español. Hydrodynamics from dissipative particle dynamics. *Physical Review E*, 52(2):1734, 1995.

[29] P. Español. *Statistical mechanics of coarse-graining*, chapter Novel Methods in Soft Matter Simulations. Springer Science & Business Media, 2004.

[30] P. Español and P. Warren. Statistical mechanics of dissipative particle dynamics. *Europhysics Letters*, 30(4):191, 1995.

[31] Mendelev et al. Interatomic potentials repository project. `http://www.ctcms.nist.gov/potentials/Download/Fe-MIM2/Fe_2.eam.fs`. Updated on 22 Dec 2010.

[32] X. Fan, N. Phan-Thien, S. Chen, X. Wu, and T. Y. Ng. Simulating flow of DNA suspension using dissipative particle dynamics. *Physics of Fluids (1994-present)*, 18(6):063102, 2006.

[33] D. A. Fedosov, G. E. Karniadakis, and B. Caswell. Dissipative particle dynamics simulation of depletion layer and polymer migration in micro-and nano-channels for dilute polymer solutions. *The Journal of Chemical Physics*, 128(14):144903, 2008.

[34] C. R. Ferguson and A. T. Kirkpatrick. *Internal Combustion Engines: Applied Thermosciences.* John Wiley and Sons, 2015.

[35] S. Fukui and R. Kaneko. Analysis of ultra-thin gas film lubrication based on linearized Boltzmann equation: First report- derivation of a generalized lubrication equation including thermal creep flow. *Journal of Tribology*, 110(2):253–261, 1988.

[36] S. Fukui and R. Kaneko. A database for interpolation of Poiseuille flow rates for high Knudsen number lubrication problems. *Journal of Tribology*, 112:78–83, 1990.

[37] J. Gao, W.D. Luedtke, and U. Landman. Layering transitions and dynamics of confined liquid films. *Physical review letters*, 79(4):705–708, 1997.

[38] J. A. Greenwood and J. H. Tripp. The contact of two nominally flat rough surfaces. *Proceedings of the Institution of Mechanical Engineers*, 1970.

[39] R. D. Groot and P. B. Warren. Dissipative particle dynamics: bridging the gap between atomistic and mesoscopic simulation. *Journal of Chemical Physics*, 107(11):4423, 1997.

[40] N. G Hadjiconstantinou. The limits of Navier-Stokes theory and kinetic extensions for describing small-scale gaseous hydrodynamics. *Physics of Fluids (1994-present)*, 18(11):111301, 2006.

[41] N. G. Hadjiconstantinou, A. L. Garcia, M. Z. Bazant, and G. He. Statistical error in particle simulations of hydrodynamic phenomena. *Journal of Computational Physics*, 187(1):274–297, 2003.

[42] B. J. Hamrock and D. Dowson. Numerical evaluation of the surface deformation of elastic solids subjected to a Hertzian contact stress. *NASA TN D-7774*, 1974.

[43] B. J. Hamrock and D. Dowson. Isothermal elastohydrodynamic lubrication of point contacts, part ii - ellipticity parameter results. *Journal of Lubrication Technology*, 98(3):375–381, 1976.

[44] B. J. Hamrock and D. Dowson. Isothermal elastohydrodynamic lubrication of point contacts, part i - theoretical formulation. *Journal of Lubrication Technology*, 98(2):223–228, 1977.

[45] C. Hijòn, P. Español, E. Vanden-Eijnden, and R. Delgado-Buscalioni. Mori-Zwanzig formalism as a practical computational tool. *Faraday Discussions*, 56:1676–1691, 1997.

[46] P. J. Hoogerbrugge and J. M. V. A. Koelman. Simulating microscopic hydrodynamic phenomena with dissipative particle dynamics. *Europhysics Letters*, 19(3):155, 1992.

[47] Y. Hu, H. S. Cheng, T. Arai, Y. Kobayashi, and S. Aoyama. Numerical solution of piston ring in mixed lubrication - a nonaxisymmetrical analysis. *Journal of Tribology*, 116(3):470–478, 1994.

[48] W. Humphrey, A. Dalke, and K. Schulten. VMD: Visual Molecular Dynamics. *Journal of Molecular Graphics*, 14(1):33–38, 1996.

[49] J. Israelachvili. *Intermolecular and surface forces*, chapter 15. Elsevier, 2011.

[50] A. Jabbarzadeh, J. D. Atkinson, and R. I. Tanner. Effects of the wall roughness on slip and rheological properties of hexadecane in molecular dynamics simulation of Couette shear flow between sinusoidal walls. *Physical review E*, 61(1):690, 2000.

[51] A. Jabbarzadeh, J. D. Atkinson, and R. I. Tanner. Effects of branching on slip and rheological properties of lubricants in molecular dynamics simulation of Couette shear flow. *Tribology International*, 35(1):35–46, 2002.

[52] S. G. Johnson. Cubature.jl. `https://github.com/stevengj/Cubature.jl`. One- and multi-dimensional adaptive integration routines for the Julia language.

[53] K. Kadau, T. C. Germann, and P. S. Lomdahl. Molecular dynamics comes of age: 320 billion atom simulation on BlueGene/L. *International Journal of Modern Physics C*, 17(12):1755–1761, 2006.

[54] E. E. Keaveny, I. V. Pivkin, M. Maxey, and G. E. Karniadakis. A comparative study between dissipative particle dynamics and molecular dynamics for simple- and complex-geometry flows. *The Journal of chemical physics*, 123(10):104107, 2005.

[55] S. Kimura, O. Aoki, H. Ogawa, S. Muranaka, and Y. Enomoto. New combustion concept for ultra-clean and high-efficiency small DI diesel engines. *SAE 1999 Transactions - Journal of Engines*, 108, 1999.

[56] Y. Kong, C. W. Manke, W. G. Madden, and A. G. Schlijper. Simulation of a confined polymer in solution using the dissipative particle dynamics method. *International Journal of Thermophysics*, 15(6):1093–1101, 1994.

[57] J. Koplik, J. R. Banavar, and J. F. Willemsen. Molecular dynamics of Poiseuille flow and moving contact lines. *Physical Review Letters*, 60:1282–1285, 1988.

[58] A. M. Kovalchenko, O. Ajayi, A. Erdemir, and G. Fenske. Friction and wear behavior of laser textured surface under lubricated initial point contact. *Wear*, 271:1719–1725, 2011.

[59] A. M. Kovalchenko, O. L. Fushchich, and S. Danyluk. The tribological properties and mechanism of wear of Cu-based sintered powdered materials containing molybdenum disulfide and molybdenum diselenite under unlubricated sliding against copper. *Wear*, 290:106–123, 2012.

[60] LAMMPS. Publications that cite lammps. `http://lammps.sandia.gov/papers.html`.

[61] U. Landman, W. D. Luedtke, and J. Gao. Atomic-scale issues in tribology: interfacial junctions and nano-elastohydrodynamics. *Langmuir*, 12(19):4514–4528, 1996.

[62] L. G. Leal. *Advanced transport phenomena: fluid mechanics and convective transport processes*, chapter 5. Cambridge University Press, 2007.

[63] J. E. Lennard-Jones. Wave functions of many-electron atoms. *Mathematical Proceedings of the Cambridge Philosophical Society*, 1931.

[64] D. Levesque and L. Verlet. Computer experiments on classical fluids. iii. time-dependent self-correlation functions. *Physcial Review A*, 2(6):2514, 1970.

[65] Y. Li. *Multiphase Oil Transport At Complex Micro Geometry.* PhD thesis, Massachusetts Institute of Technology, 2011.

[66] Y. Li, H. Chen, and T. Tian. A deterministic model for lubricant transport within complex geometry under sliding contact and its application in the interaction between the oil control ring and rough liner in internal combustion engines. *2008 SAE International Powertrains, Fuels and Lubricant Congress*, 2008.

[67] Y. Liu. Developing an approach utilizing local deterministic analysis to predict the cycle friction of the piston ring-pack in internal combustion engines. Master's thesis, Massachusetts Institute of Technology, 2013.

[68] J. Lòpez-Lemus, M. Romero-Bastida, T. A. Darden, and J. Alejandre. Liquid-vapour equilibrium of n-alkanes using interface simulations. *Molecular Physics*, 104(15):2413–2421, 2006.

[69] B. Luan and M. O. Robbins. The breakdown of continuum models for mechanical contacts. *Nature*, 435(7044):929–932, 2005.

[70] T. Lubrecht and C. H. Venner. *Multi-level methods in lubrication.* Elsevier, 2000.

[71] C. Marsh, G. Backx, and M. Ernst. Static and dynamic properties of dissipative particle dynamics. *Physcial Review E*, 56:1676–1691, 1997.

[72] M. G. Martin and J. I. Siepmann. Novel configurational-bias Monte Carlo method for branched molecules. Transferable Potentials for Phase Equilibria. 2. United-Atom description of branched alkanes. *The Journal of Physical Chemistry B*, 103(21):4508–4517, 1999.

[73] G. J. Martyna, D. J. Tobias, and M. L. Klein. Constant pressure molecular dynamics algorithms. *The Journal of Chemical Physics*, 101(5):4177–4189, 1994.

[74] M. I. Mendelev, S. Han, D. J. Srolovitz, G. J. Ackland, and D. Y. Sun. Development of new interatomic potentials appropriate for crystalline and liquid Iron. *Philosophical Magazine*, 83(35):3977–3994, 2003.

[75] Hastings mfg. Piston ring functions. `https://www.hastingsmfg.com/Race_Catalog_Pdfs/Piston_Ring_Functions.pdf`.

[76] A. Mierbach, M. L. Hildyard, D. A. Parker, and H. Xu. Piston ring performance modelling. *Proceedings of Leading Through Innovation, T&N Symposium 1995*, pages 15.1–15.13, 1995.

[77] Y. Mitsuya. Modified Reynolds equation for ultra-thin film gas lubrication using 1.5-order slip-flow model and considering surface accommodation coefficient. *Journal of Tribology*, 115(2):289–294, 1993.

[78] M. Mofijur, M. G. Rasul, J. Hyde, A. K. Azad, R. Mamat, and M. M. K. Bhuiya. Role of biofuel and their binary (diesel-biodiesel) and ternary (ethanol-biodiesel-diesel) blends on internal combustion engines emission reduction. *Renewable and Sustainable Energy Reviews*, 53:265–278, 2016.

[79] J. J. Monaghan. Smoothed particle hydrodynamics. *Annual Review of Astronomy and Astrophysics*, 30:543–574, 1992.

[80] M. H. Müser. Velocity dependence of kinetic friction in the Prandtl-Tomlinson model. *Physical Review B*, 84(12):125419, 2011.

[81] A. Niavarani and N. Priezjev. Rheological study of polymer flow past rough surfaces with slip boundary conditions. *Journal of Chemical Physics*, 129(14):144902, 2008.

[82] M. Otsuki and H. Matsukawa. Systematic breakdown of Amontons' law of friction for an elastic object locally obeying Amontons' law. *Nature Scientific Reports*, 3, 2013.

[83] A. A. Pahlavan and J. B. Freund. Effect of solid properties on slip at a fluid-solid interface. *Physical Review E*, 83(2):021602, 2011.

[84] M. Parrinello and A. Rahman. Polymorphic transitions in single crystals: a new molecular dynamics method. *Journal of Applied physics*, 52(12):7182–7190, 1981.

[85] P. Payvar and R. F. Salant. A computational method for cavitation in a wavy mechanical seal. *Journal of Tribology*, 114(1):199–204, 1992.

[86] S. Plimpton. Fast parallel algorithms for short-range molecular dynamics. *Journal of Computational Physics*, 117:1–19, 1995.

[87] S. Plimpton, P. Crozier, and A. Thompson. Lammps-large-scale atomic/molecular massively parallel simulator. *Sandia National Laboratories*, 18, 2007.

[88] M. Priest, D. Dowson, and C. M. Taylor. Theoretical modelling of cavitation in piston ring lubrication. *Proceedings of the Institution of Mechanical Engineers, Part C: Journal of Mechanical Engineering Science*, 214:435–447, 2000.

[89] N. Priezjev and S. M. Troian. Molecular origin and dynamic behavior of slip in sheared polymer films. *Physical Review Letters*, 92(1):018302, 2004.

[90] M. W. Ribarsky and U. Landman. Structure and dynamics of n-alkanes confined by solid surfaces. i. stationary crystalline boundaries. *The Journal of Chemical Physics*, 97(3):1937–1949, 1992.

[91] M. Robbins and M. Müser. *Handbook of Modern Tribology*, chapter Computer Simulations of Friction, Lubrication and Wear. CRC Press, 2000.

[92] R. E. Rudd and J. Q. Broughton. Coarse-grained molecular dynamics and the atomic limit of finite elements. *Physical Review B*, 58(10):R5893, 1998.

[93] O. S. Sankey and D. J. Niklewski. *Ab initio* multicenter tight-binding model for molecular-dynamics simulations and other applications in covalent systems. *Physical Review B*, 40:3979–3995, 1989.

[94] D. Savio, N. Fillot, and P. Vergne. A molecular dynamics study of the transition from ultra-thin film lubrication toward local film breakdown. *Tribology Letters*, 50(2):207–220, 2013.

[95] F. Schäfer and R. Van Basshuysen. *Reduced emissions and fuel consumption in automobile engines.* Springer Science and Business Media, 2013.

[96] I. Sherrington, N. Grice, and E.H. Smith. Modelling the operation of piston rings in internal combustion engines. In *NORDTRIB1990-4th Nordic Symposium on Tribology*, 1990.

[97] W. Shinoda, M. Shiga, and M. Mikami. Rapid estimation of elastic constants by molecular dynamics simulation under constant stress. *Physical Review B*, 69(13):134103, 2004.

[98] T. Soddemann, B. Dünweg, and K. Kremer. Dissipative particle dynamics: A useful thermostat for equilibrium and nonequilibrium molecular dynamics simulations. *Physical Review E*, 68:046702, 2003.

[99] Yoshio Sone. *Kinetic theory and fluid dynamics.* Springer Science & Business Media, 2012.

[100] A. Z. Szeri. *Fluid film lubrication*, chapter 2. Cambridge University Press, 2011.

[101] A. P Thompson, S. J Plimpton, and W. Mattson. General formulation of pressure and stress tensor for arbitrary many-body interaction potentials under periodic boundary conditions. *The Journal of Chemical Physics*, 131(15), 2009.

[102] P. A. Thompson and M. O. Robbins. Origin of stick-slip motion in boundary lubrication. *Science*, 250(4982):792, 1990.

[103] P. A. Thompson and M. O. Robbins. Shear flow near solids: epitaxial order and flow boundary conditions. *Physical Review A*, 41(12):6830, 1990.

[104] P. A. Thompson and S. M. Troian. A general boundary condition for liquid flow at solid surfaces. *Nature*, 389(6649):360–362, 1997.

[105] T. Tian. *Modeling the performance of the piston ring-pack in Internal Combustion engines.* PhD thesis, Massachusetts Institute of Technology, 1997.

[106] T. Tian, V. W. Wong, and J. B. Heywood. A piston ring-pack film thickness and friction model for multigrade oils and rough surfaces. *SAE Paper 962032*, 1996.

[107] M. E. Tuckerman, J. Alejandre, R. López-Rendón, A. L. Jochim, and G. J. Martyna. A Liouville-operator derived measure-preserving integrator for molecular dynamics simulations in the isothermal-isobaric ensemble. *Journal of Physics A: Mathematical and General*, 39(19):5629, 2006.

[108] L. Verlet. Computer experiments on classical fluids. i. thermodynamical properties of Lennard-Jones molecules. *Physical Review*, 159(1):98, 1967.

[109] L. Verlet. Computer experiments on classical fluids. ii. equilibrium correlation functions. *Physcial Review*, 165(1):201, 1968.

[110] E. K. Watkins and W. L. Jorgensen. Perfluoroalkanes: Conformational analysis and liquid-state properties from ab initio and Monte Carlo calculations. *The Journal of Physical Chemistry A*, 105(16):4118–4125, 2001.

[111] T. Werder, J. H. Walther, and P. Koumoutsakos. Hybrid atomistic-continuum method for the simulation of dense fluid flows. *Journal of Computational Physics*, 205:373–390, 2005.

[112] L. Wu and D. B. Bogy. A generalized compressible Reynolds lubrication equation with bounded contact pressure. *Physics of Fluids*, 13(8):2237–2244, 2001.

[113] X. Yong and L. T. Zhang. Slip in nanoscale shear flow: mechanisms of interfacial friction. *Microfluidcs Nanofluidics*, 14(1-2):299–308, 2013.

[114] S. Zhen and G. J. Davies. Calculation of the Lennard-Jones n-m potential energy parameters for metals. *Physica Status Solidi (a)*, 78(2):595–605, 1983.

[115] X. Zheng, H. Zhu, B. Kosasih, and A. K. Tieu. A molecular dynamics simulation of boundary lubrication of n-alkanes chain length and normal load. *Wear*, 301, 2013.

[116] H. T. Zhu, X. Zheng, P. B. Kosasih, and A. K. Tieu. Tribo-surface charge and polar lubricant molecules on friction and lubrication under multiple 3D asperity contacts. *Wear*, 332:1248–1255, 2015.

[117] R. Zwanzig. *Nonequilibrium statistical mechanics.* Oxford University Press, 2001.